iScience

CellPress

Article

Pyrophosphate Phosphor Solid Solution with High Quantum Efficiency and Thermal Stability for Efficient LED Lighting

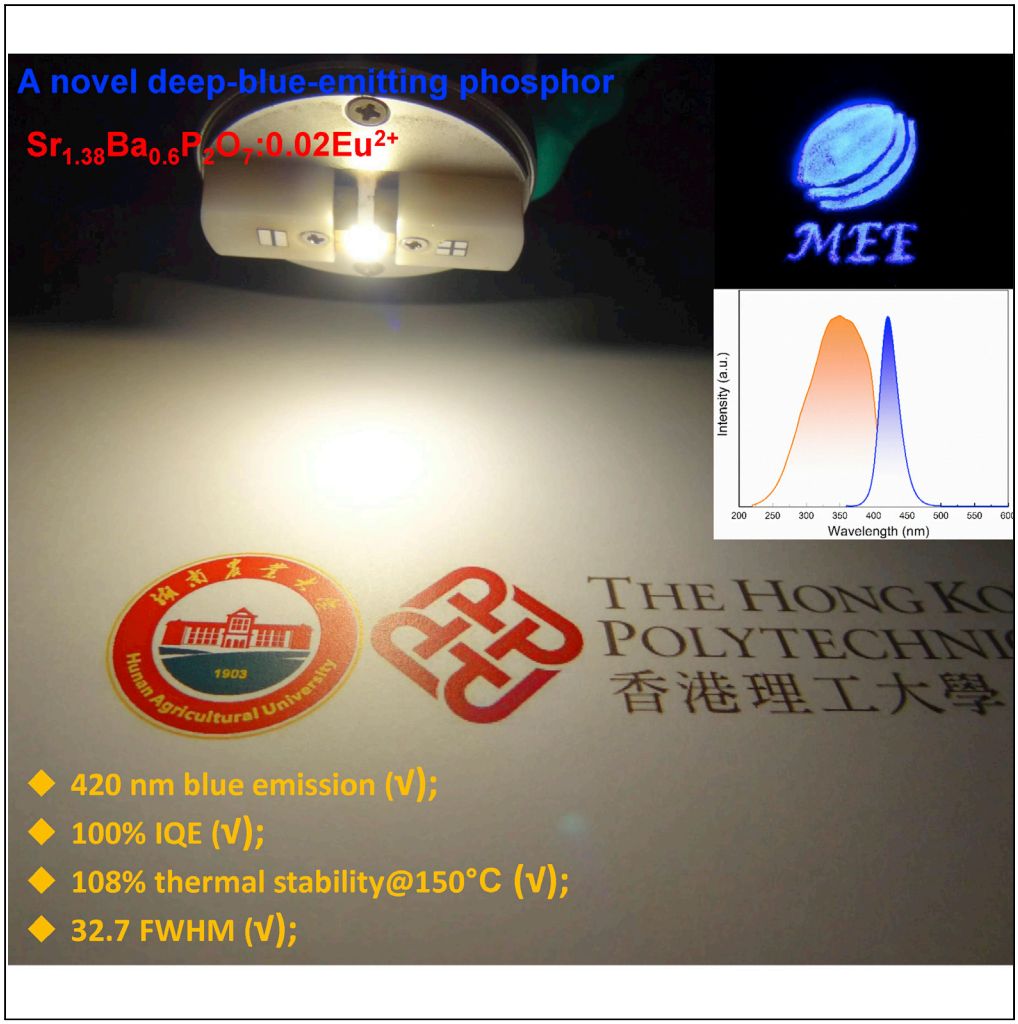

Yuan Zhong, Mao Xia, Zhi Chen, ..., Wai-Yeung Wong, Jing Wang, Zhi Zhou

wai-yeung.wong@polyu.edu.hk (W.-Y.W.)
ceswj@mail.sysu.edu.cn (J.W.)
zhouzhi@hunau.edu.cn (Z.Z.)

HIGHLIGHTS

A novel deep-blue-emitting phosphor $(Sr_{0.69}Ba_{0.3})_2P_2O_7$:0.02$Eu^{2+}$ is reported

Near-unit internal quantum efficiency is detected in $(Sr_{0.69}Ba_{0.3})_2P_2O_7$:0.02$Eu^{2}$

The thermal stability of $(Sr_{0.69}Ba_{0.3})_2P_2O_7$:0.02$Eu^{2+}$ is significantly enhanced

The application in WLEDs based on $(Sr_{0.69}Ba_{0.3})_2P_2O_7$:0.02$Eu^{2+}$ is demonstrated

Zhong et al., iScience *23*, 100892
March 27, 2020
https://doi.org/10.1016/j.isci.2020.100892

iScience

CellPress

Article

Pyrophosphate Phosphor Solid Solution with High Quantum Efficiency and Thermal Stability for Efficient LED Lighting

Yuan Zhong,[1,2,6] Mao Xia,[1,2,6] Zhi Chen,[1] Peixing Gao,[1,2] H.T. (Bert) Hintzen,[3] Wai-Yeung Wong,[4,7,*] Jing Wang,[5,*] and Zhi Zhou[1,2,*]

SUMMARY

Phosphors with high quantum efficiency and thermal stability are greatly desired for lighting industries. Based on the design strategy of solid solution, a series of deep-blue-emitting phosphors $(Sr_{0.99-x}Ba_x)_2P_2O_7$:0.02$Eu^{2+}$ (SB_xPE x = 0–0.5) are developed. Upon excitation at 350 nm, the optimized $SB_{0.3}PE$ phosphor shows a relatively narrow full width at half maximum (FWHM = 32.7 nm) peaking at 420 nm, which matches well with the plant absorption in blue region. Moreover, this phosphor exhibits obvious enhancement of internal quantum efficiency (IQE) (from 74% to 100%) and thermal stability (from 88% to 108% of peak intensity and from 99% to 124% of integrated area intensity at 150°C) compared with the pristine one. The white LED devices using $SB_{0.3}PE$ as deep-blue-emitting component show good electronic properties, indicating that $SB_{0.3}PE$ is promising to be used in plant growth lighting, white LEDs, and other photoelectric applications.

INTRODUCTION

Nowadays, artificial light has greatly lengthened daytime and changed our lifestyle (Smith, 2000; Pust et al., 2015). The advanced lighting technology and mission of saving energy require scientists to explore highly efficient luminescent materials. Phosphors, as a widely used inorganic luminescent material, play a key role in all phosphor-converted light-emitting diodes (pc-LEDs) (Ye et al., 2010). The luminescent properties of phosphors determine the performances of LED devices such as color rendering index (CRI), correlated color temperature (CCT), luminance efficiency, and service life, directly. Thus, in order to further develop the LED lighting technology, phosphors possessing better luminescent properties are highly required. Among the numerous luminescent parameters, quantum efficiency (QE) and thermal stability are recognized as the two most important indexes in most LED lighting applications (Wang et al., 2018; Shang et al., 2014; Zhao et al., 2019; Zhong et al., 2019; Song et al., 2019). On the other hand, the deep-blue-emitting phosphors, which is a significant component to improve the color rendering index of white LEDs, are rarely reported (Wang et al., 2019). Therefore, it is urgent to develop deep-blue-emitting phosphors with both higher QE and thermal stability.

Up to now, several famous blue emitters including mer-Ir(III) NHC complexes, 2,4,6-triphenylpyrimidine, $CsPbCl_3$ nanocrystals, and $(C_6H_5CH_2NH_3)_2Pb{\cdot}Br_4$ have become the research hotspots because of their low cost, high quantum efficiency, as well as super narrow emission (Nakao et al., 2017; Pal et al., 2018; Xuan et al., 2018; Gong et al., 2018; Im et al., 2011; Wang et al., 2017). However, from the viewpoint of their structure, the wet chemical approach endows serious thermal quenching property. Moreover, the usage of oleic acid (OA) and oleylamine (OLA) in the synthetic process brings intrinsic traps on their surface, making them easily decomposable even in the atmosphere. On the contrary, the inorganic phosphors generally own good QE and thermal behavior owing to their intrinsic nature of high chemical and physical stability. As for blue-emitting phosphors, $BaMgAl_{10}O_{17}:Eu^{2+}$ (BAM) is a commercialized blue-emitting phosphor. The internal quantum efficiency (IQE) and external quantum efficiency (EQE) of BAM is about 91% and 65%, respectively. To further improve the QE and thermal stability of BAM, carbon coating had been adopted by Yin et al. via chemical vapor deposition (CVD) (Yin et al., 2016). The IQE and EQE were demonstrated to increase up to 95% and 76%, and the thermal degradation decreased from 20% to 4.6%. In addition, Lin and co-workers had reported another blue phosphor $BaAl_{12}O_{19}:Eu^{2+}$ (BAO), which showed much greater thermal stability and IQE than BAM (Wei et al., 2018). However, most of commercialized blue-emitting phosphors still face serious thermal quenching. This problem should be solved for the goal of developing

[1]School of Chemistry and Materials Science, Hunan Agricultural University, Changsha 410128, P. R. China

[2]Hunan Provincial Engineering Technology Research Center for Optical Agriculture, Changsha 410128, P. R. China

[3]Section Fundamental Aspects of Materials and Energy, Delft University of Technology, Delft, the Netherlands

[4]Department of Applied Biology and Chemical Technology, The Hong Kong Polytechnic University, Hung Hom, Kowloon, Hong Kong, P. R. China

[5]State Key Laboratory of Optoelectronic Materials and Technologies, School of Chemistry, School of Materials Science and Engineering, Sun Yat-Sen University, Guangzhou 510275, P. R. China

[6]These authors contributed equally

[7]Lead Contact

*Correspondence: wai-yeung.wong@polyu.edu.hk (W.-Y.W.), ceswj@mail.sysu.edu.cn (J.W.), zhouzhi@hunau.edu.cn (Z.Z.)

https://doi.org/10.1016/j.isci.2020.100892

thermally stable blue phosphors. Recently, Kim et al. had reported a zero-thermal-quenching blue phosphor $Na_3Sc_2(PO_4)_3:Eu^{2+}$ synthesized at a relatively low temperature (Kim et al., 2017). However, the IQE of this phosphor is 74%, which needs to be further improved. For the sake of greater light quality, blue phosphors with higher QE and better thermal stability must be further developed.

In order to explore more outstanding blue phosphors, many strategies had been designed and employed by scientists. In 2014, Xie et al. developed a new technology called "Single-Particle-Diagnosis Approach" to select phosphors in a large amount of randomly synthesized bulk. Many excellent blue phosphors such as $BaSi_4Al_3N_9:Eu^{2+}$ and $Sr_3Si_{8-x}Al_xO_{7+x}N_{8-x}:Eu^{2+}$ had been found in a short time, indicating the high efficiency of this approach (Hirosaki et al., 2014). Xia et al. used "mineral learning" to design phosphor based on the existing prototype compounds (Liao et al., 2018a; Zhao et al., 2018). Recently, blue-emitting phosphor $RbNa_3(Li_3SiO_4)_4:Eu^{2+}$ was found by them. The intrinsic super narrow emission bands of these phosphors open a new avenue for high color gamut backlighting. However, their chemical stability and QE need to be further improved. "Machine learning" also has emerged as another feasible pathway to seek highly efficient phosphors. The machine-selected blue-emitting phosphor $NaBaB_9O_{15}:Eu^{2+}$ was demonstrated to possess high IQE up to 95% and good thermal stability. Nevertheless, the excitation band is centered at 275 nm and not well matched with n-UV chips (Zhuo et al., 2018; Bos, 2006). Thus, further optimizations are necessary for this phosphor and this novel intelligent method.

For a long time, solid solution design has been considered as an efficient strategy to obtain outstanding phosphors with color tunability, high QE, as well as good thermal stability (Hermus et al., 2017; Bai et al., 2015; Wang et al., 2016; Im et al., 2011). The most widely used approach involves the substitution among Ca, Sr, and Ba because of their similar alkaline earth properties (Ji et al., 2018; Lin et al., 2017). Pyrophosphate phosphor (α-$Sr_2P_2O_7:Eu^{2+}$) has been recognized as an excellent blue-emitting phosphor. Previous works mainly focused on investigating the thermoluminescence of $Sr_2P_2O_7:Cu^{2+}$, Ln^{3+} (Ln = Pr, Nd, Dy, Ho, Er and Tm); long-lasting luminescence by co-doping $M_2P_2O_7:Eu^{2+}$ (M = Ca, Sr) with other rare earth ions; the energy transfer by introducing Eu^{2+}-Mn^{2+}, Ce^{3+}-Mn^{2+}, or Tb^{3+}-Eu^{3+} into the crystal structure of $Sr_2P_2O_7$; and the luminescent properties of $Sr_2P_2O_7$ single-doped with rare earth ions (such as Eu^{2+}, Bi^{2+}, Dy^{3+}, Tb^{3+}, Sm^{3+}) (Yazici et al., 2010; Pang et al., 2009a, 2009b; Yu et al., 2017; Xu et al., 2013, 2015; Li et al., 2015; Han et al., 2015; Cao et al., 2015). Among these researches, it has proved that the traps are easily formed in α-$Sr_2P_2O_7$ host, providing a theoretical possibility to achieve superior thermal stability. The photoluminescence properties of $Sr_{2-x}Ca_xP_2O_7:Eu^{2+}$ phosphors have been investigated by Zhang et al. (Yu et al., 2012). However, the influence of Ca doping on IQE and thermal stability have not been solved. Additionally, Ba-incorporated α-$Sr_2P_2O_7:Eu^{2+}$ phosphor has not been reported so far. It is probably due to the absence of efficient emission of Eu^{2+} in the end member of σ-$Ba_2P_2O_7$. Inspired by this, in this study, solid solution pyrophosphate phosphors $(Sr_{0.99-x}Ba_x)_2P_2O_7:0.02Eu^{2+}$ (SB_xPE x = 0–0.5) have been prepared and investigated. The finally optimized $SB_{0.3}PE$ phosphor can be efficiently excited by the n-UV light and shows narrow deep blue emission (λ_{em} = 420 nm, FWHM = 32.7 nm). Moreover, a record of 100% IQE and an unexpected thermal stability (108% for peak intensity and 124% for integrated intensity at 150°C) were detected as well. These results indicate that $SB_{0.3}PE$ may be a suitable inorganic luminescent material for efficient white LED lighting.

RESULTS AND DISCUSSION

The morphology of as-prepared $Sr_{1.98}P_2O_7:0.02Eu^{2+}$ (SPE) phosphor is shown in Figure 1A. The crystal edges can be clearly distinguished, demonstrating a typical agglomeration phenomenon of crystal grains in the solid-state reaction process. In order to further confirm the existence and relative content of each element in SPE, we conducted element mapping and energy dispersive X-ray spectroscopy (EDS) on this sample. Figure 1B presents the targeted particle that we selected for element mapping analysis. As can be seen, the component elements of Sr, P, O, and Eu are homogeneously dispersed in the crystal of SPE. As shown in Figure 1C, $SB_{0.3}PE$ phosphor exhibits bright blue emission while illuminated by 365 nm light, indicating that this phosphor can be efficiently excited by commercial n-UV chips. To demonstrate the promising applications in various LED lighting applications, we have systematically investigated the luminescent properties of SB_xPE x = 0–0.5 solid solution phosphors. The corresponding photoluminescence excitation (PLE) and photoluminescence (PL) spectra of $SB_{0.3}PE$ phosphor are shown in Figure 1D. The excitation region of this series of phosphors spanned from 230 to 420 nm and was centered at 350 nm. Under the excitation at 350 nm, a characteristic $4f^65d^1 \rightarrow 4f^7$ emission band of Eu^{2+} was obtained in the range of 375–475 nm and peaked at 420 nm. The FWHM of this band is as narrow as 32.7 nm. In addition, this blue emission

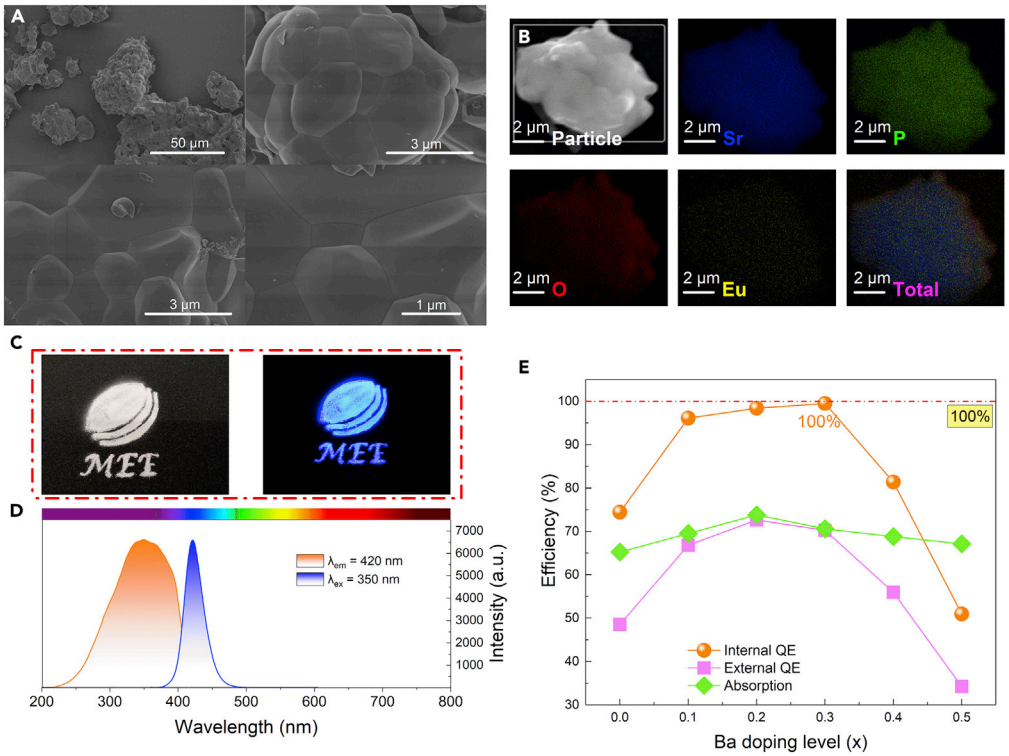

Figure 1. Micromorphology and Optical Property Characteristics

(A) SEM image of SPE phosphor.

(B) Element mapping images of selected particle, Sr, P, O, Eu, and total elements.

(C) The corresponding photographs of $SB_{0.3}PE$ phosphor under daylight and radiated by 365 nm light.

(D) PLE and PL spectra of $SB_{0.3}PE$ excited at 350 nm and monitored at 420 nm.

(E) The variations of IQE, EQE, and absorption efficiency in SB_xPE x = 0–0.5 solid solution phosphors.

Also see Figures S1–S3 and Tables S1–S3

band overlapped greatly with the absorption of Chlorophyll A, B in plants in the wavelength range of 400–460 nm (Figure S1), implying that this blue light can be used as a plant growth LED lighting source (Zhou et al., 2018). Among numerous optical properties of phosphor, quantum efficiency and thermal stability are recognized as the two most important indicators for an excellent phosphor that could be put into practical use. Accordingly, we first measured the variation of quantum efficiencies of SB_xPE (x = 0–0.5) phosphors. As shown in Figure 1E, the absorption efficiencies were kept nearly unchanged (69% in average) when the content of Ba increased from x = 0 to 0.5. However, the IQE of these phosphors was enhanced tremendously. The IQE of pristine SPE phosphor was 74%, and it was enhanced with Ba doping. The highest IQE reached up to 100% when the doping level of Ba is x = 0.3, and after that, it decreased significantly (Figure S2 and Table S1). To the best of our knowledge, such a unitive IQE has been found in blue-emitting phosphors without precedent, which is much higher than that of the commercialized ones such as $BaAl_{12}O_{19}:Eu^{2+}$ (92%), $BaMgAl_{10}O_{17}:Eu^{2+}$ (95%), and $Ba_{0.6}Sr_{1.4}SiO_4:Ce^{3+}$ (97%) (Table S2). Nevertheless, owing to the comparatively lower absorption efficiency of $SB_{0.3}PE$, the EQE (70%) is not comparable enough with these blue phosphors. The Ba doping-dependent PL spectra are presented in Figure S3A. As shown, the emission intensity of SB_xPE (x = 0–0.5) solid solution phosphors reached a maximum when the Ba doping level was x = 0.3. In this situation, the emission intensity came to 157.4% of its initial sample (SPE). With a continuing increase of the Ba content, the emission intensities dropped down quickly, matching well with the tendency observed in the IQE. However, from the viewpoint of the emission position, doping Ba into SPE's crystal structure did not alter the emission peak obviously. All the emission peaks were located at around 420 nm, and the maximal deviation of 2 nm happened in $SB_{0.2}PE$ phosphor whose emission peak is 421.5 nm (Figure S3B and Table S3). It is widely accepted that the luminescence properties of Eu^{2+}-based phosphors are easily affected by the crystal environment around it. Therefore, the nearly unchanged emission position in SB_xPE x = 0–0.5 phosphor implies that the crystal environment around the luminescence

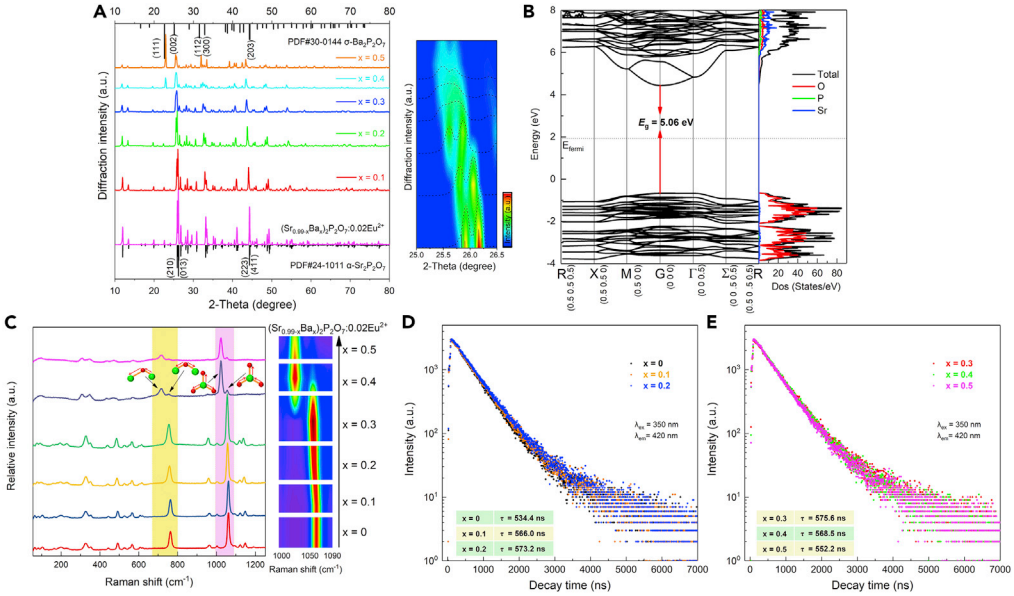

Figure 2. Crystal Phase, Band Structure, and Photoluminescence Dynamic Characteristics of SB_xPE x = 0–0.5

(A) XRD patterns of SB_xPE x = 0–0.5 solid solution (left) and magnified XRD patterns in the 2θ range of 25.0°–26.5° (right).

(B) DFT-PBE simulated electronic band structure and partial density of states (PDOS) for SPE phosphor.

(C) Resonance Raman spectra of SB_xPE x = 0–0.5 solid solution (left) and magnified Raman spectra between 1,000 and 1,090 cm^{-1} (right).

(D and E) Decay lifetimes of SB_xPE x = 0–0.5 upon the excitation of 350 nm and monitoring at 420 nm.

Also see Figures S4–S7.

centers of Eu^{2+} would not be influenced by Ba doping obviously, which may originate from the low doping level of Ba.

As we know, the structure of phosphors decides the luminescent properties directly. Thus, as a proof of concept, we first measured the X-ray diffraction (XRD) of SB_xPE (x = 0–0.5) solid solution phosphors and the corresponding patterns are shown in Figure 2A. At the first look of the XRD results we can find that the diffraction pattern of SPE sample is in accordance with its standard diffraction data (JCPDS#24-1011, α-$Sr_2P_2O_7$) (Lagos, 1970). There is no impurity or secondary phase detected implying that pure α-$Sr_2P_2O_7$ had been formed. By increasing the Ba content continuously, the characteristic diffraction peaks of (210) and (013) shifted toward lower diffraction angles, which agrees well with the Bragg's law. Moreover, we can find that another phase of σ-$Ba_2P_2O_7$ (JCPDS#30-0144) started to show up in the x = 0.4 case and dominated in x = 0.5 (Elbelghitti et al., 1995). So the solubility of Ba in α-Sr2P2O7 is about 30 mol%. The simulated crystal structures of α-$Sr_2P_2O_7$ and σ-$Ba_2P_2O_7$ are shown in Figures S4A and S4B, respectively. Typically, α-$Sr_2P_2O_7$ belongs to the orthorhombic crystal system and crystallized in the *Pnma* space group. The lattice parameters of α-$Sr_2P_2O_7$ are a = 8.9104(6), b = 5.4035(4), c = 13.1054(14) Å, α = β = γ = 90°, and V = 630.99 $Å^3$. Each P atom in α-$Sr_2P_2O_7$ is coordinated by four oxygen atoms to form [PO_4] tetrahedron. In addition, Sr atoms mainly exist in the form of nine and seven oxygen atoms coordinated [$Sr1O_9$] and [$Sr2O_7$] polyhedrons. The crystal structure of the other phase σ-$Ba_2P_2O_7$ is in a hexagonal system and crystallized in the *P-62m* space group. The lattice parameters of σ-$Ba_2P_2O_7$ are *a* = 9.415(1), *b* = 9.415(1), *c* = 7.078(1) Å, *α* = *β* = 90°, γ = 120°, and *V* = 543.35 $Å^3$. All P atoms are located in [PO_4] tetrahedrons. However, differing from Sr in α-$Sr_2P_2O_7$, Ba1 in σ-$Ba_2P_2O_7$ is coordinated by twelve oxygen atoms, whereas Ba2 is coordinated by ten oxygen atoms, forming [$Ba1O_{12}$] and [$Ba2O_{10}$] polyhedrons, respectively. Based on the similar valence states and ionic radius between Sr^{2+} ($r_{CN=9}$ = 1.36, $r_{CN=7}$ = 1.21 Å) and Eu^{2+} ($r_{CN=9}$ = 1.30, $r_{CN=7}$ = 1.20 Å), we deduce that the incorporated Eu^{2+} prefers to occupy the crystallographic sites of Sr1 in [$Sr1O_7$] polyhedrons in α-$Sr_2P_2O_7$ phase-dominated samples (SB_xPE x = 0–0.4). To have deeper insights into the band structure of SB_xPE (x = 0–0.5) solid solution, the density functional theory with Perdew-Burke-Ernzerhof (DFT-PBE) simulation was conducted using the VASP package and the related results are shown in Figures 2B and S5. The electronic band gaps for SPE, $SB_{0.3}PE$, and $SB_{0.5}PE$ were calculated to be 5.06, 5.11, and 5.06 eV, respectively. At the same time, the band structure also indicates all band gaps belong to

direct structure. The optical band gap of SB_xPE x = 0–0.5 was calculated based on the absorption data (Figure S6) as well. The values of the calculated band gap increased from 5.05 to 5.09, 5.08, 5.10, 5.08, and 5.07 eV. This variation basically agrees well with the electronic band gap calculated from DFT-PBE. In addition, the calculated density of states (DOS) of the three samples indicates that all the valence bands are dominated by the orbits of O atoms, whereas the conduction bands are composed of the orbits of O, P, Sr, and (Ba) atoms together. Therefore, the band structures are modified with the gradual doping of Ba, which would influence their optical properties.

In order to obtain more information about the molecular bonds, the measurements of Resonance Raman spectra were carried out for SB_xPE x = 0–0.5 phosphors. As shown in Figure 2C, two characteristic Raman peaks locating at 1,056 and 759 cm^{-1} are observed in the Raman spectra of SPE, which are assigned to the anti-symmetric stretching mode of PO_3 and POP in P_2O4- 7. In addition, there are three shoulder peaks located at 566, 526, and 491 cm^{-1}, corresponding to the three different deformations of δOPO, δPO_3, and δPOP, respectively. The other peaks below 400 cm^{-1} should be caused by external vibrational modes (Edhokkar et al., 2012; Seyyidoğlu et al., 2007). By increasing the Ba content in SB_xPE (x = 0–0.5) solid solution, we can observe that the peak intensities of PO_3 and POP increased as well. The peak intensity meets the maximum in $SB_{0.3}PE$ sample. However, once the Ba content exceeded 0.3, the Raman peak at 1,056 and 759 cm^{-1} suddenly decreased to the extreme low level. Astoundingly, two additional Raman peaks locating at 1,023 and 714 cm^{-1} should be attributed to the symmetric stretching mode of PO_3 and POP (Figure 2C). The mutational Raman spectra should associate with the phase transition from α-$Sr_2P_2O_7$ to σ-$Ba_2P_2O_7$, which has been confirmed by XRD measurement. It is commonly believed that the increased vibrational intensity of P-O band reflects that the connective framework of this material was increasing with Ba doping. Therefore, the intrinsic non-radiation between luminescent centers of Eu^{2+} and killer centers should be reduced, and the corresponding luminescence properties were improved. In order to further check this, the corresponding lifetimes of SB_xPE x = 0–0.5 were measured and shown in Figures 2D and 2E. Upon 350 nm excitation and 420 nm monitoring, the obtained decay data are close to a typical single exponential decay model. As can be seen, the lifetimes of SB_xPE x = 0–0.5 was lengthened with the gradual increase in the doping concentration of Ba. The longest lifetime was measured to be 575.6 ns when x was equal to 0.3, and after that, it decreased dramatically. Generally, we believe that the anisotropic substitution of Ba for Sr in SPE host would generate some defects. Furthermore, the lengthened lifetimes observed here can be assigned to the occurrence of energy transfer from these defect levels to Eu^{2+} luminescent centers. However, once the Ba content exceeds a certain content (30 mol%), the maintained energy in Eu^{2+} would further flow to the killer centers, which is the main reason accounting for the shortening of the corresponding lifetimes for $SB_{0.4}PE$ and 0.5 samples. A visual schematic was given in Figure S7 to explain the mechanism of the much improved IQE in $SB_{0.3}PE$ phosphor. Our conclusions for the improved IQE in $SB_{0.3}PE$ phosphor were subdivided into three aspects: (1) the increased Eu^{2+} concentration in each crystallographic site of Sr1. Owing to the similar valence state and effective ionic radius, the incorporated Eu^{2+} seems to still substitute Sr1. Thus, more Eu^{2+} gathered at the crystallographic sites of Sr1 in $SB_{0.3}PE$. (2) The energy transfer from the formed defects to Eu^{2+} luminescent centers. (3) The enhanced connective framework induced less energy transfer from Eu^{2+} to killer centers. Therefore, by the co-working of the above three effects, the emission intensity and QE in $SB_{0.3}PE$ reached the maximum.

Another key factor affecting the electronic luminescence (EL) of LED devices is the thermal stability of phosphors. Generally, the working temperature of pc-LEDs could reach up to 150°C or higher. Herein, the impact of Ba doping on the thermal stability of SPE was investigated as well. As shown in Figures 3A and 3B, the emission intensity of SPE declined remarkably as the environmental temperature rose from the natural condition to 200°C. At 150°C, SPE phosphor can maintain about 88% (for peak intensity) and 99% (for integrated area intensity) of its initial emission intensity, implying a comparable thermal behavior of commercialized $BaMgAl_{10}O_{17}:Eu^{2+}$ phosphor (Wei et al., 2018; Figure 3C). Although the thermal stability of SPE is almost satisfied for practical applications, the 30 mol% Ba-substituted phosphor shows a greater thermal behavior, which reached up to 108% (for peak intensity) and 124% (for integrated area intensity) at 150°C, respectively. More interestingly, the emission intensity of this phosphor experienced an up-and-down process, which is totally different from the pristine SPE phosphor. Figure S8 displays the corresponding temperature-dependent excitation spectrum of $SB_{0.3}PE$ phosphor. Same as the temperature-dependent emission of this phosphor, the excitation intensity enhanced until the temperature reached 125°C and then dropped rapidly. However, the rise in temperature would not cause obvious shift in the excitation spectra, indicating the stable crystal environment of the luminescent centers of Eu^{2+} in $SB_{0.3}PE$ (Figure S8B).

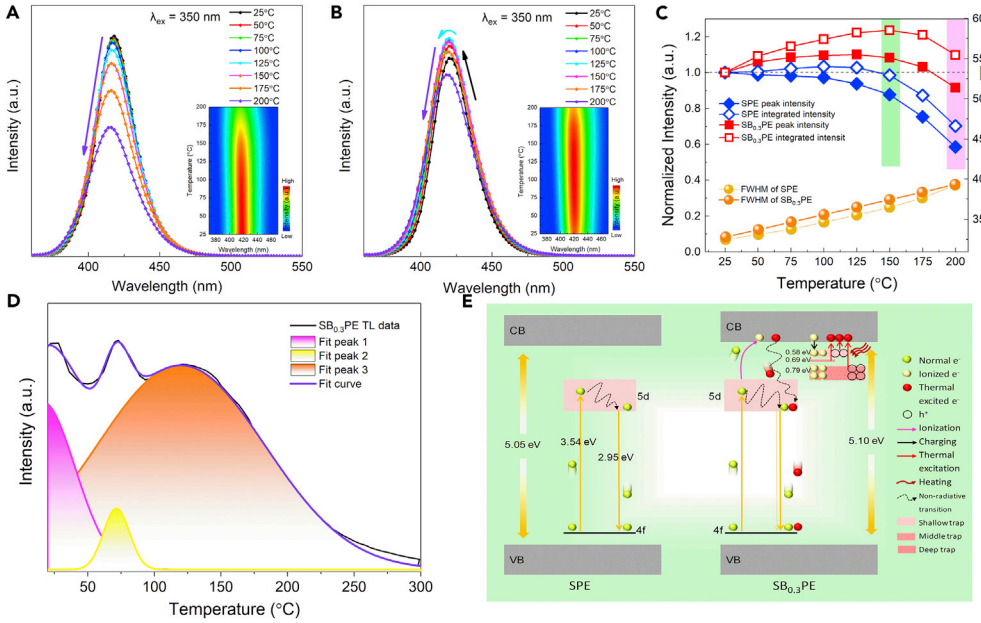

Figure 3. Improved Thermal Stability Performance of $SB_{0.3}PE$ and the Related Mechanism

(A and B) Temperature-dependent emission spectra of SPE and $SB_{0.3}PE$.

(C) The relationship of peak and integrated intensity, FWHM of SPE, and $SB_{0.3}PE$ versus different temperatures.

(D) TL spectra of $SB_{0.3}PE$.

(E) Proposed mechanism for improved thermal stability in $SB_{0.3}PE$ phosphor.

Also see Figures S8–S11.

According to the literature, the amazing improved thermal stability may be associated with the formation of some trap levels created by Ba doping and can be evidenced by thermal luminescence (TL) measurement, which would be discussed below (Kim et al., 2017). The FWHM increased from 32.5 to 39.2 nm for SPE and from 32.8 to 39.3 nm for $SB_{0.3}PE$. In addition, we have checked the temperature-dependent decay times of SPBE x = 0.3. As shown in Figure S9A, the lifetimes started to extend from 25°C (337.3 ns) and met the maximum at 125°C (352.1 ns), very close to the law that temperature-dependent PL shows. The prolonged lifetime demonstrates that the energy transferred from the trap levels that were formed by Ba doping to the luminescent centers, and this effect should benefit the thermal stability of this phosphor because Eu^{2+} can transfer more energy into efficient radiations. However, the lifetime declined unusually at relatively higher temperature. To further check the origin of this result, the temperature-dependent PLE and PL spectra and the corresponding magnified plot were given in Figures S10A and S10B, respectively. Intriguingly, the emission band become more and more broader, causing the increase of FWHM, which has been illustrated in Figure 3C. The low-energy tail in temperature-dependent PLE showed a red shift, whereas the high-energy tail in temperature-dependent PL spectra located more in the blue region. The overlap area got larger, demonstrating a more serious reabsorption in this phosphor. Therefore, the decline of lifetime should be assigned to the enhanced reabsorption in $SB_{0.3}PE$ at higher temperature (Liao et al., 2019). However, the IQE and EQE decreased monotonously. At 150°C, the IQE and EQE is 85% and 60%, respectively (Figures S9B and S9C). The observed decreases of IQE and EQE are linked with the energy storage of these traps rather than direct emission. The thermal degradation of $SB_{0.3}PE$ was also checked by heating and cooling the sample for several times. As shown in Figure S11A, after cooling the sample back to room temperature, the emission intensity abnormally increased up to 120%, 138%, and 141% for cycles 1, 2, and 3. This unnatural discovery needs to be resolved in the future works. Moreover, this phosphor possesses good irradiant stability at high temperature. The emission intensity varied less than 0.7% at 150°C even after continuously being irradiated for 4 h (Figure S11B).

To further confirm the existence of traps levels in $SB_{0.3}PE$ phosphor, the TL spectrum was measured. As shown in Figure 3D, the TL curve exhibited three obvious peaks in the temperature range of 20°C –300°C. By using Gaussian fitting, three individual peaks locating at 15.6, 71.5, and 119.9°C emerged. Thus, the corresponding trap depths (ET) were calculated to be 0.58, 0.69, and 0.79 eV according to the

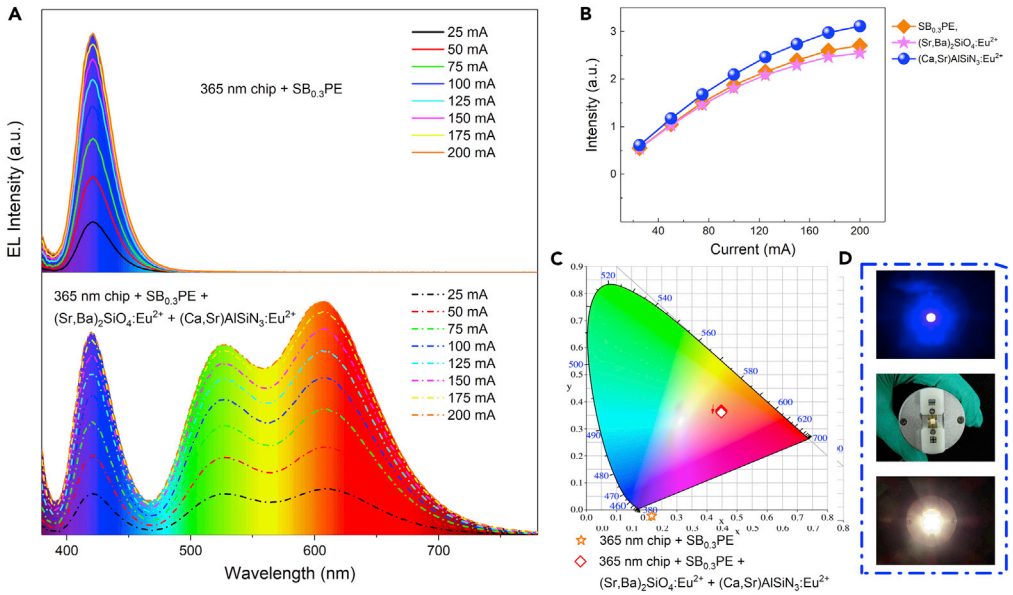

Figure 4. Performance of as-fabricated pc-LED Devices

(A) The emission spectra of fabricated plant growth LED (up) and white LED (down) driven at various currents.

(B) The emission intensities of blue, green, and red phosphors as a function of driving current.

(C) CIE chromaticity coordinate of plant growth LED and white LED under different current driving conditions.

(D) The corresponding photographs of plant growth LED (driven), white LED, and driven white LED.

Also see Table S4.

empirical equation ET = T/500 eV (Zhuo et al., 2018; Ding and Wang, 2017; Liao et al., 2018b; Qiao et al., 2019). Moreover, Dorenbos also proposed a classical model to explain the thermal quenching phenomenon of Eu^{2+}-activated phosphors, which illustrated that the excited electrons in the 5d level could be thermally excited into the conduction band (CB) and finally quenched in it. The thermal stability of phosphor depends on the energy gap between 5d level and CB ($E_{5d\text{-}CB}$) (Qiao et al., 2019). The smaller the value of this energy is, the more serious the thermal quenching would be. However, both the integrated emission intensities of SPE and $SB_{0.3}PE$ did not drop by 50% even at 200°C, and this reflects that this model should not be the main working mechanism for the thermal quenching in these phosphors.

It is essential to comprehensively realize the mechanism of the greatly improved thermal stability in $SB_{0.3}PE$ phosphor. Here, we give our explanation and put it in Figure 3E. First, in SPE phosphor, the electrons in Eu^{2+} can be excited by n-UV light from 4f to 5d energy level. The excited electrons directly relax to the lowest 5d level and then return to 4f ground state through a classical 5d → 4f transition. However, in $SB_{0.3}PE$ phosphor, the excited electrons in 5d level will go through an additional ionization approach to be further excited into the conduction band (CB). Then, these electrons will be charged into three kinds of traps. These traps are located at different energy positions. The larger the ET is, the deeper the position these traps are located at. When the environmental temperature increased, the charged electrons could be thermally re-excited by recombining with the inherent holes in traps. Through CB and the non-radiative process, these thermally excited electrons reach the lowest 5d level, followed by $4f^6 5d^1 \rightarrow 4f^7$ transition to return to the ground state. In this process, the thermally quenched emission could be compensated by the additional 5d → 4f transitions of Eu^{2+}. Therefore, the thermal stability of $SB_{0.3}PE$ phosphor has been improved by this thermal activated process.

The unprecedented IQE, thermal stability, relatively narrow FWHM, as well as the plant absorption-matched emission band indicate that $SB_{0.3}PE$ phosphor has promising applications in plant growth lighting and white LEDs. To demonstrate this, we have fabricated a series of plant growth LED and white LED. The plant growth LED combined $SB_{0.3}PE$ blue-emitting phosphor with the commercial 365-nm chip directly, whereas other white LEDs were fabricated by blending $SB_{0.3}PE$ deep-blue phosphor, green-emitting $(Sr,Ba)_2SiO_4:Eu^{2+}$ phosphor (λ_{em} = 524 nm), and red-emitting $(Ca,Sr)AlSiN_3$ phosphor (λ_{em} = 610 nm) as trichromatic emitters. Figure 4A shows the emission spectra of as-fabricated plant growth LED and white

LED under different current driven conditions. By increasing the driving current, the emission intensities of two LED devices increased simultaneously. As for white LED, the intensities of blue, green, and red light emitted from trichromatic phosphors were enhanced constantly, indicating a comparable stability of $SB_{0.3}PE$ with these commercial phosphors (Figure 4B). Figure 4C shows the CIE coordinates of plant growth LED and white LED driven by different currents. The CIE coordinates of plant growth LED remained stable, whereas the white LED shifted from (0.3958, 0.4065) to (0.3958, 0.3984) (Table S4). Figure 4D presents the photographs of our fabricated plant growth LED and white LED. Driven under a current of 25 mA, the plant growth LED shows deep blue emission and the CIE coordinates are located at (0.1660, 0.0155). For white LED, the CIE coordinates are (0.3958, 0.4065). Moreover, a relatively high CRI of 86.8, low CCT of 3831 K as well as a high luminance efficiency of 45.9 $lm \cdot W^{-1}$ were obtained as well.

Conclusions

In summary, we have developed a deep-blue-emitting phosphor of $SB_{0.3}PE$ from SB_xPE x = 0–0.5 solid solution with high IQE and thermal stability. This phosphor possesses a narrow FWHM of 32.7 nm, and its blue emission at 420 nm matches well with plant's absorption. The IQE of $SB_{0.3}PE$ phosphor is as high as 100%, which is record to the best of our knowledge. In addition, $SB_{0.3}PE$ possesses fascinating thermal stability. It can maintain 108% of the initial peak intensity and 124% of the integrated area intensity at 150°C, which is much better than most of other commercial blue phosphors. Thus, the suitable emission range, narrow FWHM, unprecedented IQE, as well as superior thermal stability allow $SB_{0.3}PE$ to be promisingly applied in plant growth lighting, white LED, and other related photoelectric fields.

Limitations of the Study

The absorption efficiency of phosphors is another key parameter to affect its EQE. Although in this study the best IQE reached up to 100%, the absorption efficiency is still limited at 71% and did not change much with the co-doping of Ba. Therefore, the value of EQE needs to be further optimized by improving the absorption efficiency.

METHODS

All methods can be found in the accompanying Transparent Methods supplemental file.

SUPPLEMENTAL INFORMATION

Supplemental Information can be found online at https://doi.org/10.1016/j.isci.2020.100892.

ACKNOWLEDGMENTS

This work was financially supported by the National Natural Science Foundation of China (Grant Nos. 51974123, 21706060, 51703061), the Hunan Graduate Research and Innovation Project (Grant No. CX2018B396), the Hunan Provincial Engineering Technology Research Center for Optical Agriculture (Grant No. 2018TP2003), and the Research Foundation of Hunan Agricultural University (Grant No. 19QN11), W.-Y.W. thanks the financial support from the Hong Kong Polytechnic University (1-ZE1C) and Ms Clarea Au for the Endowed Professorship in Energy (847S).

AUTHOR CONTRIBUTIONS

Y.Z. and M.X. conceived this strategy and launched this project. Y.Z. and P.G. synthesized all the materials and conducted experimental characterizations. Z.C. carried out the DFT-PBE calculations and analyzed these data. Y.Z., M.X., and Z.Z. contributed to the construction of luminescence mechanism. W.-Y.W., J.W., and Z.Z. supervised this project and prepared the manuscript with assistance from all other co-authors. All authors have given approval to the final version of the manuscript.

DECLARATION OF INTERESTS

The authors declare no competing interests.

Received: December 26, 2019
Revised: January 14, 2020
Accepted: February 4, 2020
Published: March 27, 2020

REFERENCES

Bai, G.X., Tsang, M.K., and Hao, J.H. (2015). Tuning the luminescence of phosphors: beyond conventional chemical method. Adv. Opt. Mater. *3*, 431.

Bos, A.J.J. (2006). Theory of thermoluminescence. Radiat. Meas. *41*, S45.

Cao, R.P., Cao, C.Y., Yu, X.G., Li, W.S., and Qiu, J.R. (2015). Photoluminescence of $Sr_2P_2O_7$:Sm^{3+} phosphor as reddish orange emission for white light-emitting diodes. Int. J. Appl. Ceram. Technol. *12*, 755–759.

Ding, X., and Wang, Y.H. (2017). Commendable Eu^{2+} doped oxide based matrix-$LiBa_{12}(BO_3)_7F_4$ red broad emission phosphor excited by NUV light: electronic and crystal structures, luminescence properties. ACS Appl. Mater. Interfaces *9*, 23983–23994.

Edhokkar, F., Hadrich, A., Graiab, M., and Mhiri, T. (2012). $Ba_{1.01}Sr_{0.99}P_2O_7$: un nouveau site Ba^{2+} révélé par diffraction des rayons X. Acta Crystallogr. C Struct. Chem. *C68*, i86–i88.

Elbelghitti, A.A., Elmarzouki, A., Boukhari, A., and Holt, E.M. (1995). α-Dibarium pyrophosphate. Acta Crystallogr. C Struct. Chem. *C51*, 1478–1480.

Gong, X.W., Voznyy, O., Jain, A., Liu, W.J., Sabatini, R., Piontkowski, Z., Walters, G., Bappi, G., Nokhrin, S., Bushuyev, O., et al. (2018). Electron–phonon interaction in efficient perovskite blue emitters. Nat. Mater. *17*, 550–556.

Han, B., Li, P.J., Zhang, J.T., Zhang, J., Xue, Y.F., and Shi, H.Z. (2015). The effect of Li^+ ions on the luminescent properties of a single-phase white light-emitting phosphor α-$Sr_2P_2O_7$:Dy^{3+}. Dalton Trans. *44*, 7854–7861.

Hermus, M., Phan, P.C., Duke, A.C., and Brgoch, J. (2017). Tunable optical properties and increased thermal quenching in the blue-emitting phosphor series: $Ba_2(Y_{1-x}Lu_x)_5B_5O_{17}$:$Ce^{3+}$ (x = 0–1). Chem. Mater. *29*, 5267–5275.

Hirosaki, N., Takeda, T., Funahashi, S., and Xie, R.-J. (2014). Discovery of new nitridosilicate phosphors for solid state lighting by the single-particle-diagnosis approach. Chem. Mater. *26*, 4280–4288.

Im, W.B., George, N., Kurzman, J., Brinkley, S., Mikhailovsky, A., Hu, J., Chmelka, B.F., DenBaars, S.P., and Seshadri, R. (2011). Efficient and color-tunable oxyfluoride solid solution phosphors for solid-state white lighting. Adv. Mater. *23*, 2300–2305.

Ji, X.Y., Zhang, J.L., Li, Y., Liao, S.Z., Zhang, X.G., Yang, Z.Y., Wang, Z.L., Qiu, Z.X., Zhou, W.L., Yu, L.P., et al. (2018). Improving quantum efficiency and thermal stability in blue-emitting $Ba_{2-x}Sr_xSiO_4$:Ce^{3+} phosphor via solid solution. Chem. Mater. *30*, 5137–5147.

Kim, Y.H., Arunkumar, P., Kim, B.Y., Unithrattil, S., Kim, E., Moon, S.H., Hyun, J.Y., Kim, K.H., Lee, D., Lee, J.S., et al. (2017). A zero-thermal-quenching phosphor. Nat. Mater. *16*, 543–551.

Lagos, C.C. (1970). Luminescence of divalent europium in Ba-Ca, Ba-Sr, and Ca-Sr orthophosphate and pyrophosphate compositions. J. Electrochem. Soc. *117*, 1189–1193.

Li, L.Y., Peng, M.Y., Viana, B., Wang, J., Lei, B.F., Liu, Y.L., Zhang, Q.Y., and Qiu, J.R. (2015). Unusual concentration induced antithermal quenching of the Bi^{2+} emission from $Sr_2P_2O_7$:Bi^{2+}. Inorg. Chem. *54*, 6028–6034.

Liao, H.X., Zhao, M., Molokeev, M.S., Liu, Q.L., and Xia, Z.G. (2018a). Learning from a mineral structure toward an ultra-narrow-band blue-emitting silicate phosphor $RbNa_3(Li_3SiO_4)_4$:Eu^{2+}. Angew. Chem. Int. Ed. *57*, 11728–11731.

Liao, S.Z., Ji, X.Y., Liu, Y.F., and Zhang, J.L. (2018b). Highly efficient and thermally stable blue-green $(Ba_{0.8}Eu_{0.2}O)(Al_2O_3)_{4.575\times(1+x)}$ phosphor through structural modification. ACS Appl. Mater. Interfaces *10*, 39064–39073.

Liao, H.X., Zhao, M., Zhou, Y.Y., Molokeev, M., Liu, Q.L., Zhang, and Xia, Z.G. (2019). Polyhedron transformation toward stable narrow-band green phosphors for wide-color-gamut liquid crystal display. Adv. Funct. Mater. *29*, 1901988.

Lin, C.C., Tsai, Y.T., Johnston, H.E., Fang, M.H., Yu, F.J., Zhou, W.Z., Whitfield, P., Li, Y., Wang, J., Liu, R.-S., et al. (2017). Enhanced photoluminescence emission and thermal stability from introduced cation disorder in phosphors. J. Am. Chem. Soc. *139*, 11766–11770.

Nakao, K., Sasabe, H., Komatsu, R., Hayasaka, Y., Ohsawa, T., and Kido, J. (2017). Significant enhancement of blue OLED performances through molecular engineering of pyrimidine-based emitter. Adv. Opt. Mater. *5*, 1600843.

Pal, A.K., Krotkus, S., Fontani, M., Mackenzie, C.F.R., Cordes, D.B., Slawin, A.M.Z., Samuel, I.D.W., and Colman, E.Z. (2018). High-efficiency deep-blue-emitting organic light-emitting diodes based on iridium(III) carbene complexes. Adv. Mater. *31*, 1804231.

Pang, R., Li, C.Y., Shi, L.L., and Su, Q. (2009a). A novel blue-emitting long-lasting pyrophosphate phosphor $Sr_2P_2O_7$:Eu^{2+}, Y^{3+}. J. Phys. Chem. Sol. *70*, 303–306.

Pang, R., Li, C.Y., Zhang, S., and Su, Q. (2009b). Luminescent properties of a new blue long-lasting phosphor $Ca_2P_2O_7$:Eu^{2+}, Y^{3+}. Mater. Chem. Phys. *113*, 215–218.

Pust, P., Schmidt, P.J., and Schnick, W. (2015). A revolution in lighting. Nat. Mater. *14*, 454–458.

Qiao, J.W., Zhou, G.J., Zhou, Y.Y., Zhang, Q.Y., and Xia, Z.G. (2019). Divalent europium-doped near-infrared-emitting phosphor for light-emitting diodes. Nat. Commun. *10*, 5267.

Seyyidoğlu, S., Özenbaş, M., Yazıcı, N., and Yılmaz. (2007). Investigation of solid solution of ZrP_2O_7-$Sr_2P_2O_7$. J. Mater. Sci. *42*, 6453–6463.

Shang, M.M., Li, C.X., and Lin, J. (2014). How to produce white light in a single-phase host? Chem. Soc. Rev. *43*, 1372–1386.

Smith, H. (2000). Phytochromes and light signal perception by plants-an emerging synthesis. Nature *407*, 585–591.

Song, E.H., Han, X.X., Zhou, Y.Y., Wei, Y., Jiang, X.-F., Ye, S., Zhou, B., Xia, Z.G., and Zhang, Q.Y. (2019). Long-lived photon upconversion phosphorescence in $RbCaF_3$:Mn^{2+},Yb^{3+} and the dynamic color separation effect. iScience *19*, 597–606.

Wang, C.-Y., Takeda, T., Kate, O.M., Funahashi, S., Xie, R.-J., Takahashi, K., and Hirosaki, N. (2019). New deep-blue-emitting Ce-doped $A_{4-m}BnC_{19+2m}X_{29+m}$ (A = Sr, La; B = Li; C = Si, Al; X = O, N; $0 \leq m \leq 1$; $0 \leq n \leq 1$) phosphors for high color-rendering warm white light-emitting diodes. ACS Appl. Mater. Interfaces *11*, 29047–29055.

Wang, L., Xie, R.-J., Li, Y.Q., Wang, X.J., Ma, C.-G., Luo, D., Takeda, T., Tsai, Y.T., Liu, R.-S., and Hirosaki, N. (2016). $Ca_{1-x}Li_xAl_{1-x}Si_{1+x}N_3$:$Eu^{2+}$ solid solutions as broadband color-tunable and thermally robust red phosphors for superior color rendition white light-emitting diodes. Light Sci. Appl. *5*, e16155.

Wang, L., Xie, R.-J., Suehiro, T., Takeda, T., and Hirosaki, N. (2018). Down-conversion nitride materials for solid state lighting: recent advances and perspectives. Chem. Rev. *118*, 1951–2009.

Wang, Z.F., Yuan, F.L., Li, X.H., Li, Y.C., Zhong, H.Z., Fan, L.S., and Yang, S.H. (2017). 53% efficient red emissive carbon quantum dots for high color rendering and stable warm white-light- emitting diodes. Adv. Mater. *29*, 1702910.

Wei, Y., Cao, L., Lv, L., Li, G.G., Hao, J.R., Gao, J.S., Su, C.C., Lin, C.C., Jang, H.S., Dang, P.P., et al. (2018). Highly efficient blue emission and superior thermal stability of $BaAl_{12}O_{19}$:Eu^{2+} phosphors based on highly symmetric crystal structure. Chem. Mater. *30*, 2389–2399.

Xu, M.J., Wang, L.X., Jia, D.Z., and Zhao, H.Y. (2015). Tuning the color emission of $Sr_2P_2O_7$: Tb^{3+}, Eu^{3+} phosphors based on energy transfer. J. Am. Ceram. Soc. *98*, 1536–1541.

Xu, M.J., Wang, L.X., Jia, D.Z., Liu, L., Zhang, L., Guo, Z.P., and Sheng, R. (2013). Morphology tunable self-assembled $Sr_2P_2O_7$:Ce^{3+}, Mn^{2+} phosphor and luminescence properties. J. Am. Ceram. Soc. *96*, 1198–1202.

Xuan, T.T., Lou, S.Q., Huang, J.J., Cao, L.Y., Yang, X.F., Li, H.L., and Wang, J. (2018). Monodisperse and brightly luminescent $CsPbBr_3/Cs_4PbBr_6$ perovskite composite nanocrystals. Nanoscale *10*, 9840–9844.

Yazici, A.N., Seyyidoğlu, S., Toktamiş, H., and Yilmaz, A. (2010). Thermoluminescent properties of $Sr_2P_2O_7$ doped with copper and some rare earth elements. J. Lumin. *130*, 1744–1749.

Ye, S., Xiao, F., Pan, Y.X., Ma, Y.Y., and Zhang, Q.Y. (2010). Phosphors in phosphor-converted white light-emitting diodes: recent advances in materials, techniques and properties. Mater. Sci. Eng. R *71*, 1–34.

Yin, L.J., Dong, J.T., Wang, Y.P., Zhang, B., Zhou, Z.Y., Jian, X., Wu, M.Q., Xu, X., Ommenc, J.R., and

Hintzend, H.T. (2016). Enhanced optical performance of $BaMgAl_{10}O_{17}:Eu^{2+}$ phosphor by a novel method of carbon coating. J. Phys. Chem. C *120*, 2355–2361.

Yu, J.Y., Zhang, X., Hao, Z.D., Luo, Y.S., Wang, X.J., and Zhang, J.H. (2012). Blue emission of $Sr_{2-x}Ca_xP_2O_7:Eu^{2+}$ for near UV excitation. J. Alloys Compd. *515*, 39–43.

Yu, S.Z., Wang, D., Wu, C.F., and Wang, Y.H. (2017). Synthesis and control the morphology of $Sr_2P_2O_7:Eu^{2+}/Eu^{2+}$, Mn^{2+} phosphors by precipitation method. Mater. Res. Bull. *93*, 83–90.

Zhao, M., Liao, H.X., Molokeev, M.S., Zhou, Y.Y., Zhang, Q.Y., Liu, Q.L., and Xia, Z.G. (2019). Emerging ultra-narrow-band cyan-emitting phosphor for white LEDs with enhanced color rendition. Light Sci. Appl. *8*, 1–9.

Zhao, M., Liao, H.X., Ning, L.X., Zhang, Q.Y., Liu, Q.L., and Xia, Z.G. (2018). Next-generation narrow-band green-emitting $RbLi(Li_3SiO_4)_2:Eu^{2+}$ phosphor for backlight display application. Adv. Mater. *30*, 1802489.

Zhong, Y., Gai, S.J., Xia, M., Gu, S.M., Zhang, Y.L., Wu, X.B., Wang, J., Zhou, N., and Zhou, Z. (2019). Enhancing quantum efficiency and tuning photoluminescence properties in far-red-emitting phosphor $Ca_{14}Ga_{10}Zn_6O_{35}:Mn^{4+}$ based on chemical unit engineering. Chem. Eng. J. *374*, 381–391.

Zhou, Z., Zhong, Y., Xia, M., Zhou, N., Lei, B.F., Wang, J., and Wu, F.F. (2018). Tunable dual emission of $Ca_3Al_4ZnO_{10}:Bi^{3+},Mn^{4+}$ via energy transfer for indoor plant growth lighting. J. Mater. Chem. C *6*, 8914–8922.

Zhuo, Y., Tehrani, A.M., Oliynyk, A.O., Duke, A.C., and Brgoch, J. (2018). Identifying an efficient, thermally robust inorganic phosphor host via machine learning. Nat. Commun. *9*, 4377.

iScience, Volume *23*

Supplemental Information

Pyrophosphate Phosphor Solid Solution with High Quantum Efficiency and Thermal Stability for Efficient LED Lighting

Yuan Zhong, Mao Xia, Zhi Chen, Peixing Gao, H.T. (Bert) Hintzen, Wai-Yeung Wong, Jing Wang, and Zhi Zhou

Supplemental information

Pyrophosphate phosphor solid solution with high quantum efficiency and thermal stability for efficient LED lighting

Yuan Zhong,[1,2,6] Mao Xia,[1,2,6] Zhi Chen,[1] Peixing Gao,[1,2] H. T. (Bert) Hintzen,[3] Wai-Yeung Wong,[4,7,*] Jing Wang,[5,*] Zhi Zhou,[1,2,*]

[1]School of Chemistry and Materials Science, Hunan Agricultural University, Changsha 410128, P. R. China.

[2]Hunan Provincial Engineering Technology Research Center for Optical Agriculture, Changsha 410128, P. R. China.

[3]Section Fundamental Aspects of Materials and Energy, Delft University of Technology, The Netherlands.

[4]Department of Applied Biology and Chemical Technology, The Hong Kong Polytechnic University, Hung Hom, Kowloon, Hong Kong, P. R. China.

[5]State Key Laboratory of Optoelectronic Materials and Technologies, School of Chemistry, School of Materials Science and Engineering, Sun Yat-Sen University, Guangzhou 510275, P. R. China.

[6]These authors equally contributed to this work.

[7]Lead Contact

*Correspondence: wai-yeung.wong@polyu.edu.hk (W.-Y.W.)
ceswj@mail.sysu.edu.cn (J.W.)
zhouzhi@hunau.edu.cn (Z.Z.)

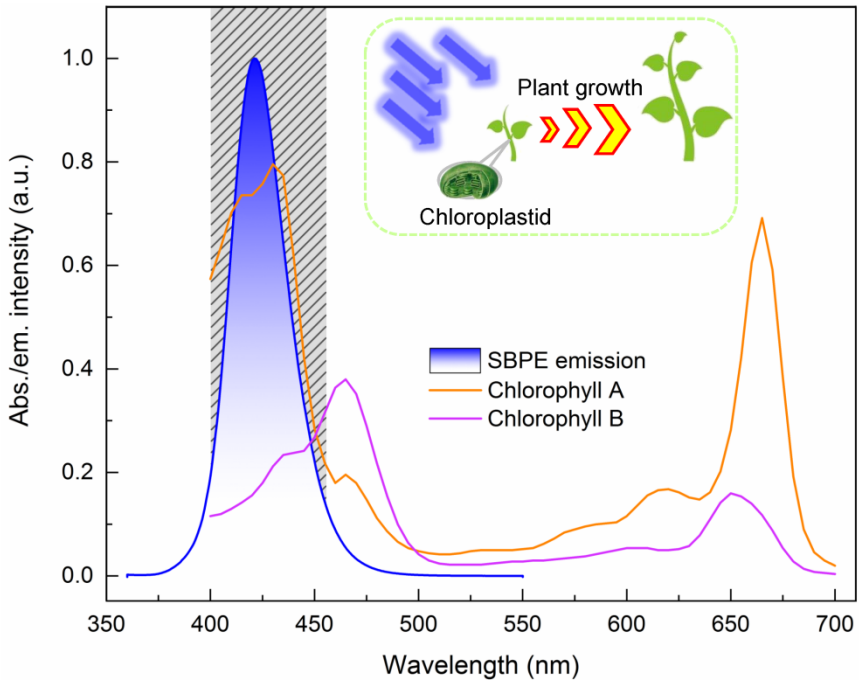

Figure S1. A comprehensive comparison between the emission band of SB_xPE x = 0-0.5 phosphor and the absorption spectra of Chlorophyll A and B, and the inset shows that this blue light can be absorbed by Chloroplastid to accelerate plant growth. Related to Figure 1.

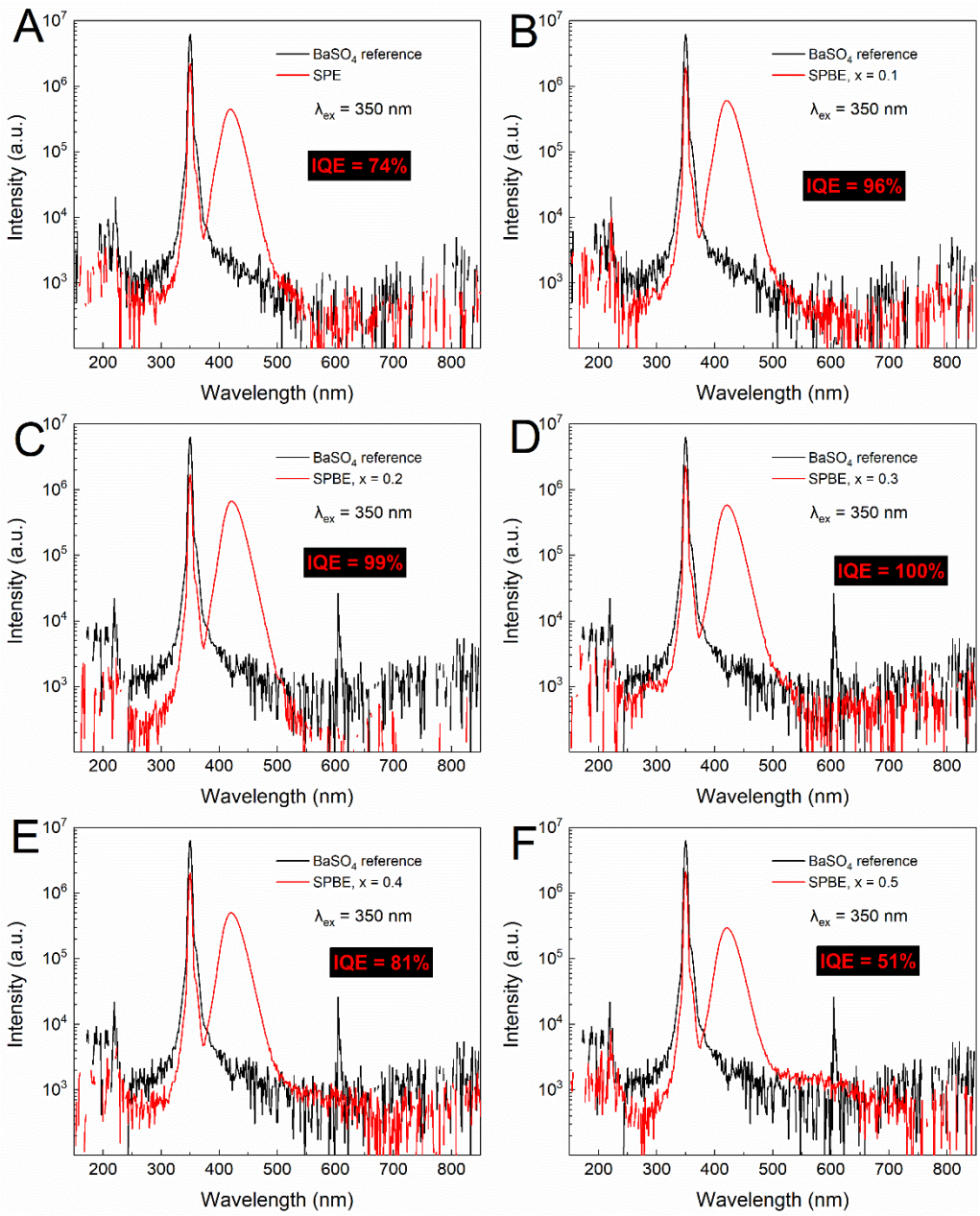

Figure S2. The corresponding IQE measurements of SB_xPE x = 0-0.5 phosphors. Related to Figure 1.

Our measurements of quantum efficiencies were carried out on a QE-2100 quantum efficiency testing system (Otsuka, Japan) with a heat apparatus. An integrating sphere of 6 inches in diameter was used to integrate the excitation and emission intensity. $BaSO_4$ powders were employed to calculate the absorption photons as a reference. In addition, the external (η_0), internal (η_i) and absorption ($\alpha_{abs.}$) efficiencies were calculated using the following equations (Wang et al., 2015):

$$\eta_0 = \frac{\int \lambda * P(\lambda) d\lambda}{\int \lambda * E(\lambda) d\lambda}, \eta_{\mathrm{i}} = \frac{\int \lambda * P(\lambda) d\lambda}{\int \lambda \{E(\lambda) - R(\lambda)\} d\lambda}, \alpha_{\mathrm{abs.}} = \frac{\int \lambda \{E(\lambda) - R(\lambda)\} d\lambda}{\int \lambda * E(\lambda) d\lambda} \quad (1)$$

where $P(\lambda)$, $E(\lambda)$ and $R(\lambda)$ are the photon quantity in the emission, excitation and reflection spectrums, respectively. Moreover, each sample was re-excited to obtain the corrected absolute internal and external quantum efficiencies.

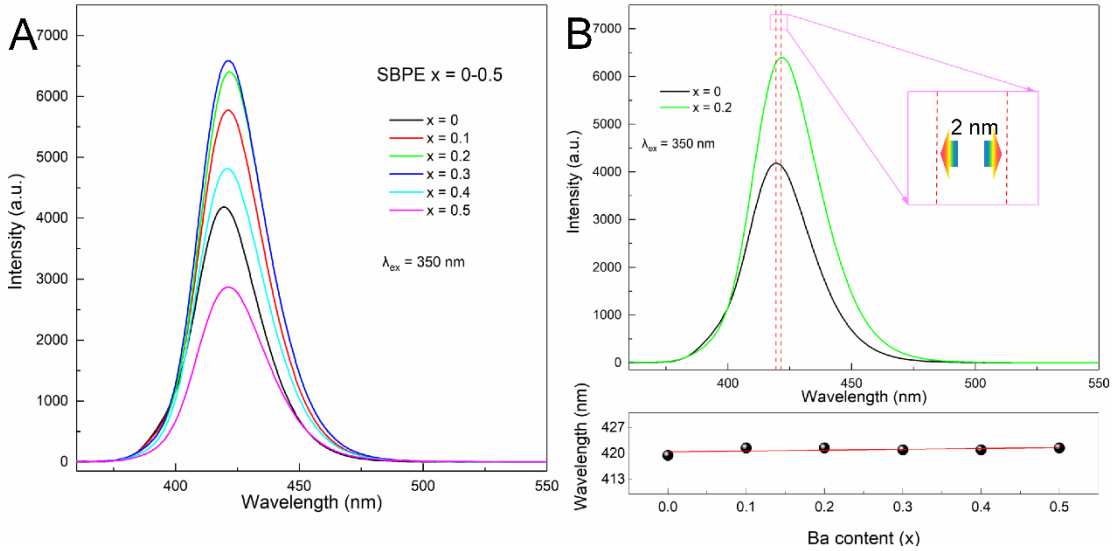

Figure S3. (A) Emission spectra of SB_xPE x = 0-0.5 under 350 nm excitation. (B) The red shift in the emission spectra between x = 0 and x = 0.2 samples (up) and the variations of emission peak of SB_xPE x = 0-0.5 solid solution (down). Related to Figure 1.

Table S1. The variations of IQE, EQE and absorption efficiency in SB_xPE x = 0-0.5 solid solution phosphors. Related to Figure 1.

Ba content	IQE (measured)	IQE (corrected)	EQE (measured)	EQE (corrected)	Absorption
x = 0	76%[a)]	74%	50%	49%	65%
	76%[b)]	74%	49%	48%	65%
	76[c)]±0.03%[d)]	74±0.10%	49.5±0.04%	48.5±0.10%	65±0.05%
x = 0.1	98%	96%	68%	67%	70%
	98%	96%	68%	67%	70%
	98±0.12%	96±0.13%	68±0.08%	67±0.09%	70±0.01%

	100%	99%	74%	73%	74%
x = 0.2	100%	99%	74%	73%	74%
	100±0.15%	99±0.14%	74±0.04%	73±0.09%	74±0.02%
	102%	100%	72%	71%	71%
x = 0.3	101%	100%	71%	70%	70%
	101.5±0.26%	100±0.19%	71.5±0.12%	70.5±0.21%	70.5±0.08%
	83 %	81%	57%	56%	69%
x = 0.4	83%	82%	57%	56%	69%
	83±0.17%	81.5±0.21%	57±0.07%	56±0.09%	69±0.06%
	53%	51%	35%	34%	67%
x = 0.5	52%	51%	35%	34%	67%
	52.5±0.19%	51±0.03%	35±0.17%	34±0.03%	67±0.09%

a), b), c) and d) denote the first, second, calculated average data and standard deviation of QE.

Table S2. Crystal structures and PL properties of several highly efficient blue-emitting phosphors reported so far. Related to Figure 1.

Phosphor compound	Crystal structure	Space group	λ_{ex} (nm)	λ_{em} (nm)	EQE	IQE	Ref.
$RbNa_3(Li_3SiO_4)_4:Eu^{2+}$	tetragonal	*I4/m*	400	471	13%	53%	(Zhao et al., 2018)
$Na_3Sc_2(PO_4)_3:Eu^{2+}$	monoclinic	*C2/c*	370	453	64%	74%	(Kim et al., 2017)
$NaSrBO_3:Ce^{3+}$	monoclinic	*$P2_1/c$*	355	420	62%	75%	(Liu et al., 2011)
$NaCaBO_3:Ce^{3+}$	orthorhombic	*Pmmn(59)*	347	421	-	75%	(Zhang et al., 2014)
$SrLu_2O_4:Ce^{3+}$	orthorhombic	*Pnam(64)*	390	460	-	76%	(Zhang et al., 2017)
$K_2BaCa(PO_4)_2:Eu^{2+}$	trigonal	*P-3m1*	350	460	-	83%	(Qiao et al., 2018)
$La_3Si_{6.5}Al_{1.5}N_{9.5}O_{5.5}:Ce^{3+}$	monoclinic	*I2/a*	355	425	54%	84%	(Wang et al., 2017)

$BaAl_{12}O_{19}:Eu^{2+}$	hexagonal	*P6₃/mmc*	350	445	-	92%	(Wei et al., 2018)
$Li_4SrCa_{0.97}(SiO_4)_2:Ce^{3+}$	orthorhombic	*Pbcm*	362	413	-	94%	(Zhang et al., 2015)
$BaMgAl_{10}O_{17}:Eu^{2+}$	hexagonal	*P6₃/mmc*	310	458	76%	95%	(Yin et al., 2016)
$Ba_{0.6}Sr_{1.4}SiO_4:Ce^{3+}$	orthorhombic	*Pmcn/Pmnb*	360	411	81%	97%	(Ji et al., 2018)
SB_xPE x =0.3	orthorhombic	*Pnma*	350	420	70%	100%	This work

Table S3. PLE and PL peak positions, FWHM and Stokes shifts of SB_xPE x = 0-0.5 solid solution phosphors. Related to Figure 1.

Compound	PLE peak (nm)	PL peak (nm)	FWHM (nm)	Stokes shift (cm^{-1})[a)]
SPE	352.0	419.5	32.4	4571.2
SB_xPE x =0.1	351.5	420.5	32.6	4668.3
SB_xPE x =0.2	351.0	421.5	32.7	4765.2
SB_xPE x =0.3	350.0	420.0	32.7	4761.9
SB_xPE x =0.4	348.0	420.0	33.0	4926.1
SB_xPE x =0.5	347.5	421.5	33.9	5052.2

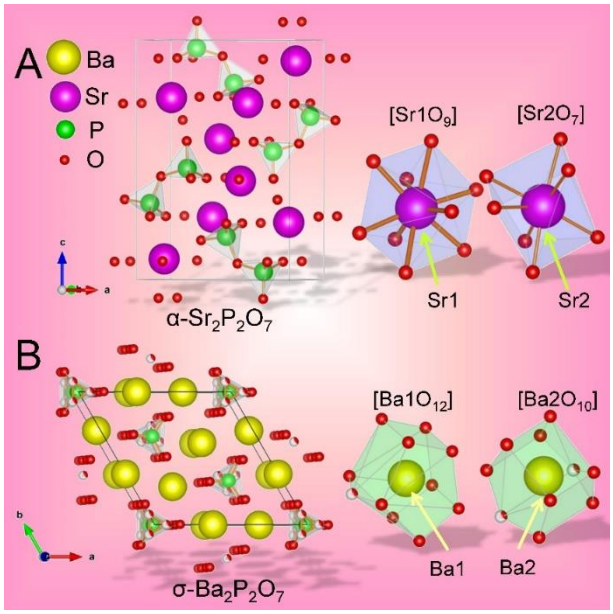

Figure S4. The crystal structure of α-$Sr_2P_2O_7$ (A) and σ-$Ba_2P_2O_7$ (B). The yellow, purple, green and red balls represent Ba, Sr, P and O atoms, respectively. The right in

(A) shows seven oxygen atoms coordinated [Sr_1O_9] and [Sr_2O_7] polyhedrons in α-$Sr_2P_2O_7$. In addition, ten oxygen and twelve oxygen atoms coordinated [$Ba1O_{12}$] and [$Ba2O_{10}$] polyhedrons in σ-$Ba_2P_2O_7$ are shown in the right of (B). Related to Figure 2.

The expected crystallographic site for the incorporated Eu^{2+} to substitute in SB_xPE x = 0-0.5 was inferred according to the following equation proposed by Van Uitert (Van Uitert, 1984; Chen et al., 2017; Chen et al., 2017):

$$E = Q\left[1 - \left(\frac{V}{4}\right)^{1/V} 10^{-nE_a r/80}\right] \qquad (2)$$

where *E* is the edge position of 5d energy level of Eu^{2+} in this case, *Q* presents the lowest energy position of 5d energy level (here *Q* equals to 34 000 cm^{-1} for Eu^{2+}), *V* stands for the valence state of Eu (*V* = 2 for Eu^{2+}), *n* denotes the coordinating anions number of Eu^{2+}, *r* is the cation's radius which is expected to substitute Eu^{2+} in phosphor, E_a is the electron affinity of the phosphors. As for phosphate phosphors, E_a is equal to 2.19 eV. On the basis of the above equation and data, we estimated the values of *E* for the cases of Eu^{2+} substituting the crystallographic sites of Sr1 (CN = 9) and Sr2 (CN = 7) in α-$Sr_2P_2O_7$ phase dominated samples (SB_xPE *x* = 0-0.4), Ba1 (CN = 12) and Ba2 (CN = 10) in σ-Ba_2P_2O phase dominated sample (SB_xPE *x* = 0.5), respectively. The calculated energy values of *E* for Sr1, Sr2, Ba1 and Ba2 are 19904, 22885, 26887 and 24777 cm^{-1}, respectively. Therefore, according to these data, the theoretical emission positions for Eu^{2+} substituting Sr1, Sr2, Ba1 and Ba2 are 502 nm, 437 nm, 404 nm and 372 nm, respectively. It should be pointed out that both 437 nm and 404 nm emission are very close to the practical emission peak (420 nm) obtained from our experiences. Thus, we believe that the doped Eu^{2+} ions are preferred to occupy the crystallographic sites of Sr2 in α-$Sr_2P_2O_7$ based samples (*x* = 0-0.4) and Ba1 in σ-$Ba_2P_2O_7$ based sample (*x* = 0.5).

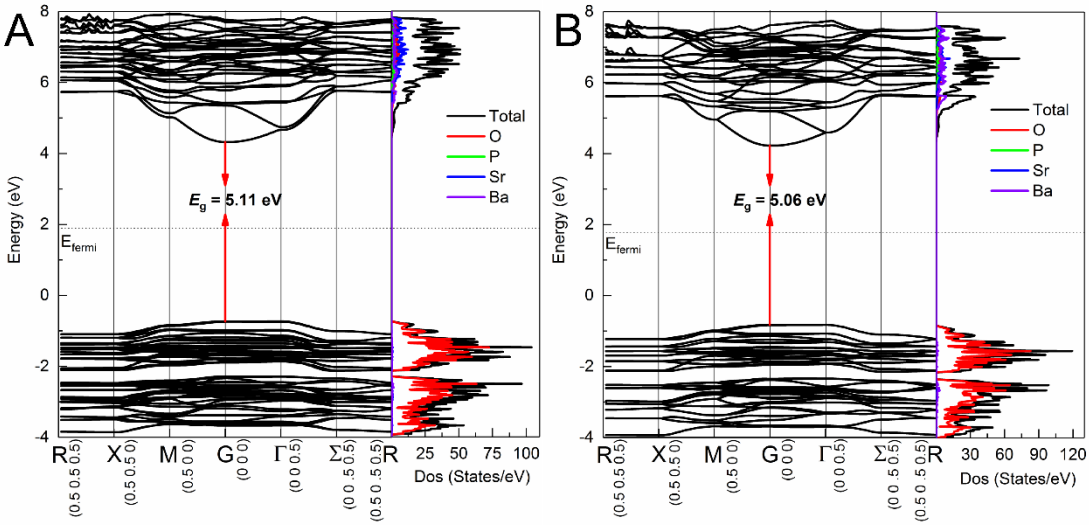

Figure S5. Electron band structure, total and orbital densities of states of $SB_{0.3}PE$ (A)

and $SB_{0.5}PE$ (B) phosphor calculated using DFT-PBE code in the VASP package. Related to Figure 2.

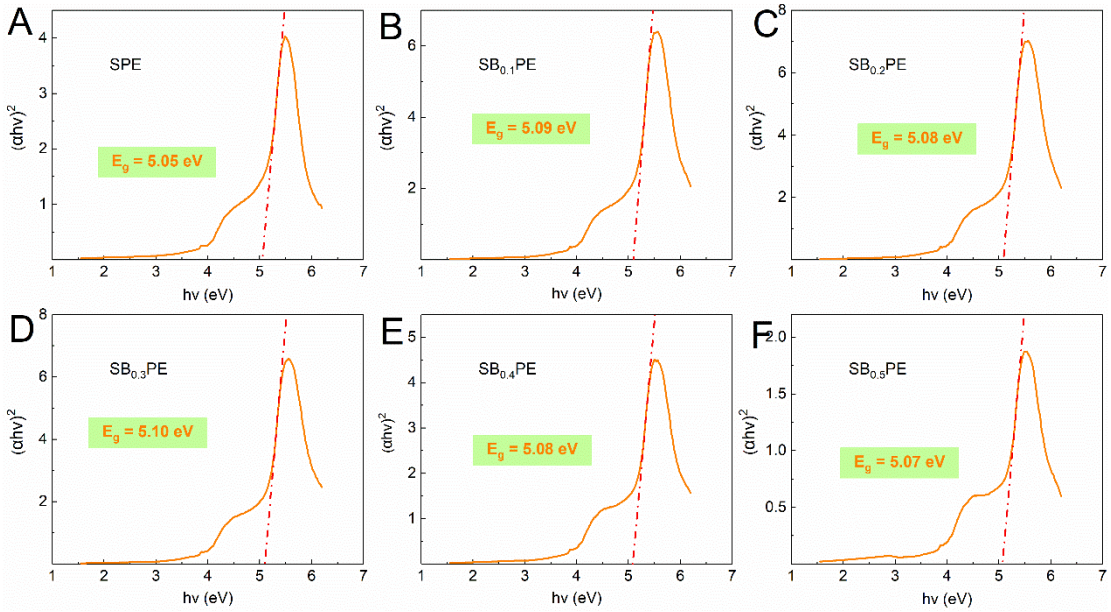

Figure S6. The corresponding band gap calculations for SB_xPE x = 0-0.5 solid solution. Related to Figure 2.

The optical band gaps were calculated using UV-vis absorption data. The relative equation which was proposed by Tauc, Davis, and Mott is expressed as follows (Mott et al., 1979):

$$(\alpha hv)^{1/n} = A(hv - E_g) \qquad (3)$$

where *h*, *v*, *α*, *A* and E_g are Planck's constant, frequency of vibration, absorption coefficient, proportional constant and the band gap energy. Here, n stands for the nature of electron transitions. When *n* = 1/2 and 2 denote the direct and indirect allowed transition, whereas *n* = 3/2 and 3 denote the direct and indirect forbidden transition, respectively. From the VASP stimulated band structure we found that both the minimum energy in conduction band and the maximum energy in valence band are located at the same k-point in Brillouin zone. Thus, for SB_xPE x = 0-0.5 solid solution phosphors, the value of n should be 1/2. Moreover, the relationship between *hv* and *λ* is (William et al., 2007):

$$hv = 1239.7/\lambda \qquad (4)$$

The above plots were drawn using 1239.7/*λ* as x axis and $\left(\frac{1239.7}{\lambda}\alpha\right)^2$ as y axis. A tangent line was plotted at the point of inflection. Then, the obtained intercept at x axis is just the optical band gap energy.

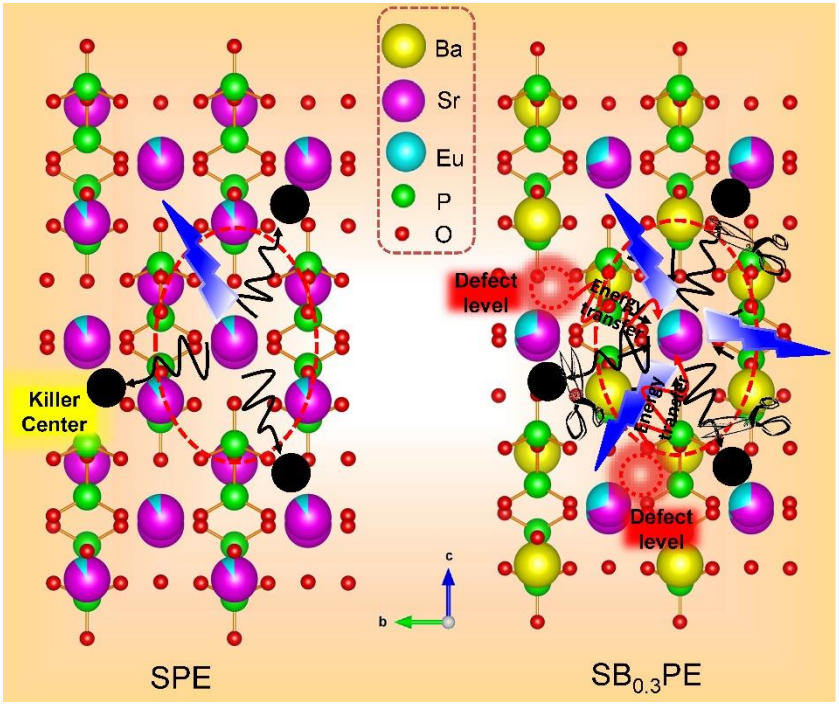

Figure S7. Schematic diagram of the significantly enhanced IQE in $SB_{0.3}PE$ phosphor. Related to Figure 2.

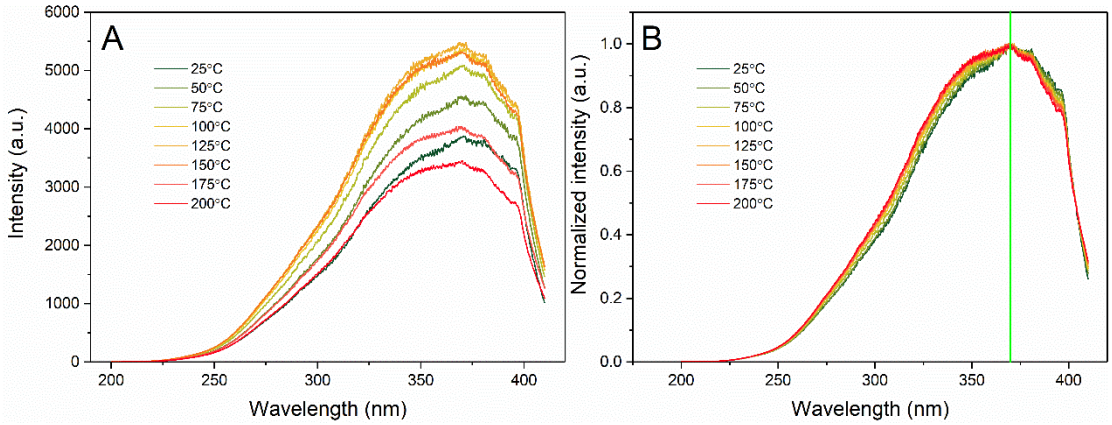

Figure S8. (A) The temperature-dependent excitation spectrum of $SB_{0.3}PE$ under the monitoring at 420 nm. (B) The normalized temperature-dependent excitation spectrum. Related to Figure 3.

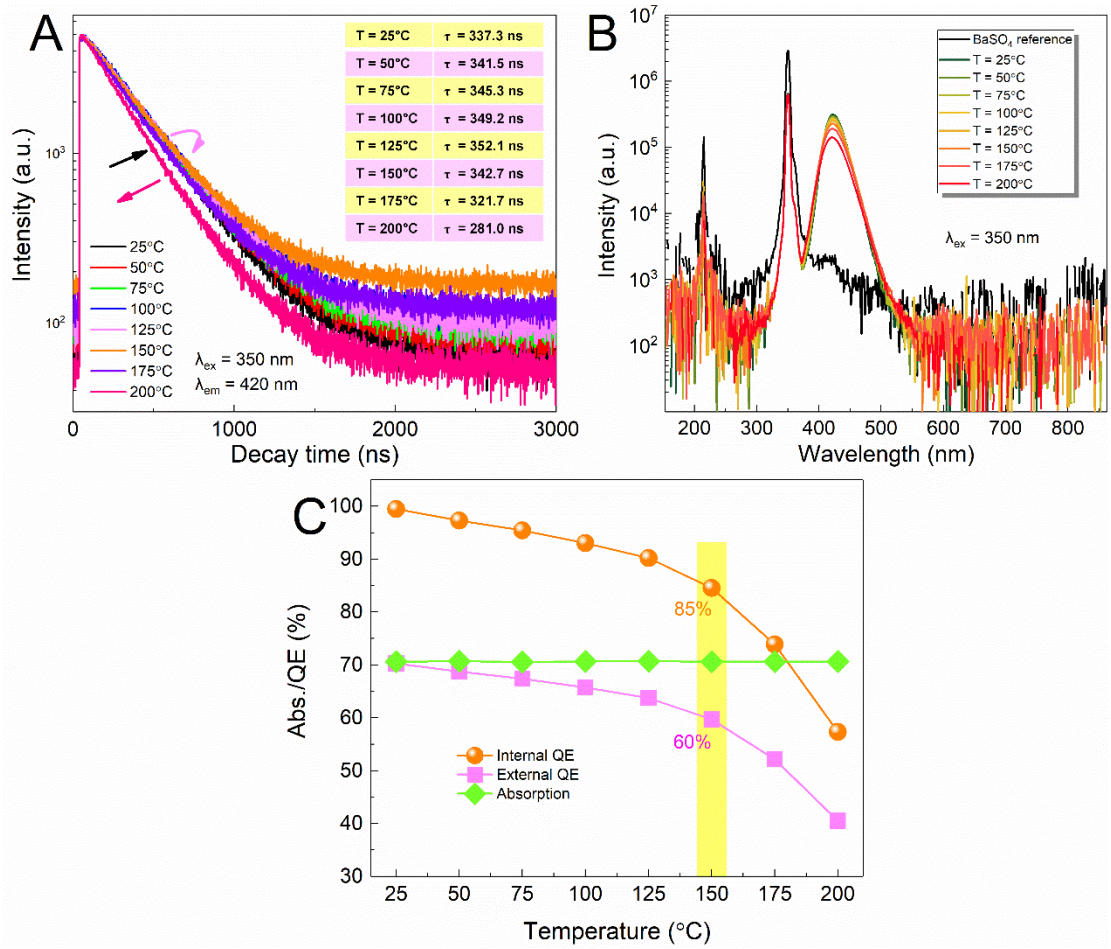

Figure S9. (A) Temperature-dependent decay times of $SB_{0.3}PE$ phosphor upon the excitation at 350 nm and monitoring at 420 nm. (B) Temperature-dependent IQE under 350 nm excitation. (C) The variations of IQE, EQE and absorption efficiency versus temperature from 25°C to 200°C. Related to Figure 3.

For temperature-dependent PL, decay times as well as QE measurements, the temperature all rose from 25°C to 200°C with an interval of 25°C. All the measurements were conducted until the temperature was stabilized for 10 minutes. All the temperature-dependent decay data were fitted by the typical single-exponential decay mode, which is expressed as follows (Blasse et al., 1994):

$$I_{(t)} = I_0 + A * exp(-t/\tau) \quad (5)$$

where $I_{(t)}$, I_0 are the luminescence intensity of phosphors at time t and 0, respectively. *A* stands for a constant value and τ is the decay time.

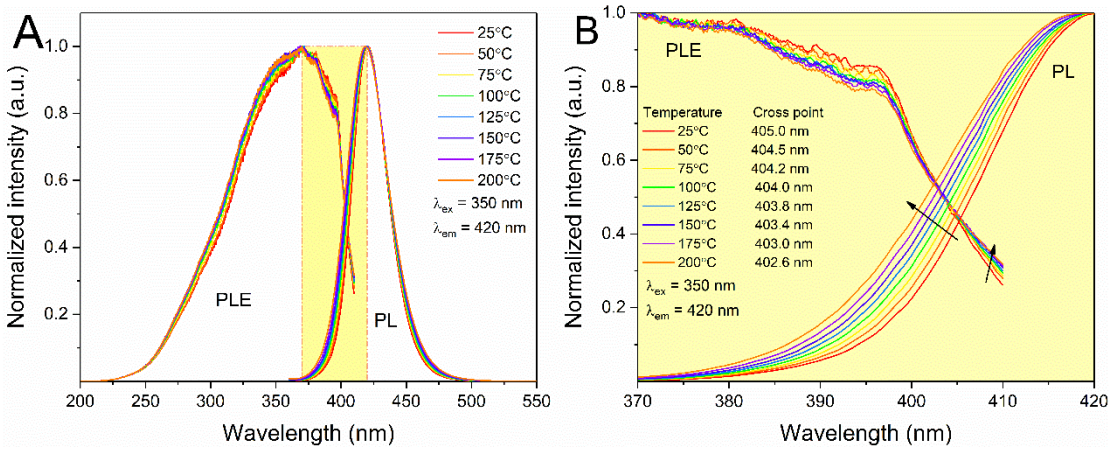

Figure S10. (A) The normalized temperature-dependent PLE and PL spectra of SB0.3PE phosphor. (B) the magnified temperature-dependent PLE and PL spectra in the wavelength range of 370-420 nm. Related to Figure 3.

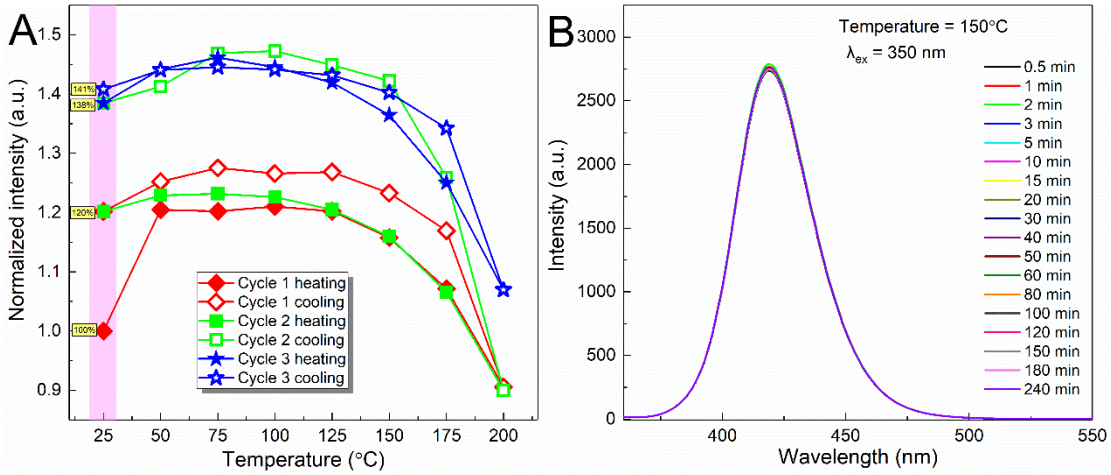

Figure S11. (A) Thermal degradation tests of $SB_{0.3}PE$ phosphor by heating and cooling phosphor for 3 times. (B) High-temperature (150°C) PL spectra of $SB_{0.3}PE$ phosphor irradiated with 350 n-UV light for several minutes. Related to Figure 3.

Table S4. EL properties of plant growth LED and white LED devices fabricated using $SB_{0.3}PE$ phosphor as the blue-emitting component. Related to Figure 4.

LED devices	Current (mA)[a)]	CCT (K)	CIE (x, y)	R_a	Luminous efficacy ($lm \cdot W^{-1}$)
Plant growth LED	25	10000	(0.1660, 0.0155)	-	1.96
	50	10000	(0.1659, 0.0155)	-	1.90
	75	10000	(0.1658, 0.0156)	-	1.76
	100	10000	(0.1656, 0.0157)	-	1.64
	125	10000	(0.1656, 0.0159)	-	1.53
	150	10000	(0.1654, 0.0160)	-	1.44
	175	10000	(0.1653, 0.0162)	-	1.34
	200	10000	(0.1652, 0.0164)	-	1.24
BGR-white LED	25	3831	(0.3958, 0.4065)	86.8	45.90
	50	3823	(0.3957, 0.4050)	87.1	45.64
	75	3814	(0.3957, 0.4036)	87.1	43.23
	100	3811	(0.3956, 0.4028)	87.3	40.85
	125	3807	(0.3955, 0.4019)	87.4	38.66
	150	3799	(0.3955, 0.4008)	87.6	36.50
	175	3789	(0.3956, 0.3997)	87.6	34.34
	200	3775	(0.3958, 0.3984)	87.7	32.24

[a)] All data were collected under the constant current conditions.

Transparent Methods

Synthesis of materials: Solid solution phosphors SB_xPE x = 0-0.5 were prepared through high temperature solid-state reaction method. The analytical reagents of $SrCO_3$ (Aladdin), $BaCO_3$ (Aladdin), $NH_4H_2PO_4$ (Aladdin) and Eu_2O_3 (99.99%, Aladdin) were used as raw materials. The doping level of Eu^{2+} in phosphors was fixed at 0.02.

Typically, stoichiometric amounts of raw materials were weighted and put in an agate mortar. The mixtures were ground thoroughly for 30 min and several drops of ethyl alcohol were added to disperse the powders. For further firing process, these samples were firstly sintered at 600°C in a N_2 flow (180 ml min^{-1}) for 5 h in a horizontal tube furnace. Then, heating of the samples was continued up to 1200°C and the temperature was maintained for 5 h. The output rate of 20 ml·min^{-1} H_2 (N_2 : H_2 = 90% : 10%) was conducted at the last 2 hours of heating to reduce Eu^{3+} in europium oxide. Finally, after the samples were naturally cooled down to room temperature, they were crushed to fine powders and stored in a chamber at the constant temperature and humidity for further measurements.

Sample characterization: The XRD data were collected in the 2θ range of 10°-80° on a Rigaku D/Max-2200 X-ray diffractometer with Cu-Kα radiation (λ = 1.5406 Å) and 40 kV operating voltage and 40 mA operating current. The scan speed was set as 6° min^{-1} and 0.02° per step. The morphologies of phosphors were checked on a dual-beam electron microscope (FEI helios nanolab G3 UC), operating at the SE mode. The attached energy dispersive X-ray spectrometer (EDS) was used to detect the elementary component and distribution. The PLE and PL spectra were recorded on an F-4700 spectrometer (Hitachi, Japan) and a 150 W Xe lamp was used as the excitation source. The temperature-dependent emission spectra were recorded on the same apparatus with a heat controller (TAP-02, China) to manipulate the temperature range from 25°C to 200°C with the heating rate of 100 °C·min^{-1} and 25°C heating step. UV–vis absorption spectra were obtained from U-3310 spectrophotometer (Hitachi, Japan) attached with a $BaSO_4$-based integrating sphere. The room-temperature and temperature-dependent quantum efficiencies were collected on QE-2100 quantum efficiency testing system (Otsuka, Japan) with a heat apparatus. Resonance Raman spectra were acquired on inVia Qontor confocal Raman microscope (Renishaw, UK) operated with 532 nm green laser and 1250-55 cm^{-1} scanning range. The room and temperature-dependent lifetimes were collected on a FLS920 spectrometer (Edinburgh, UK) and Xe900 lamp was used as the excitation source. TL spectra were measured on a FJ-427A1 microcomputer TL dosimeter (Beijing Nuclear Instrument Factory) operated at a heating rate of 4 °C·s^{-1}. The sample was preheated before TL measurement and radiated under 254 nm and 365 nm UV light for 5 min each. All photographs were taken using a DSC-HX10 digital camera (Sony, Japan).

Computation details: For the theoretical simulation section, the density functional theory (DFT) calculations were successfully implemented by employing the Vienna ab initio simulation package (VASP) as the computing equipment. Generally, the Perdew-Burke-Ernzerhof (PBE) function in generalized gradient approximation (GGA) was adopted to carry out the geometry optimization and band computations (Kresse et al., 1996; Kresse et al, 1999; Perdew et al., 1996; Qiao et al., 2019; Qiao et al., 2019). The plane-wave energy cutoff was set as 500 eV and the calculations stopped until the total energy and the forces applied on each atom converged to 10^{-5} eV and 10^{-2} eV·Å^{-1}, respectively. In the band structure calculations, a 3 × 6 × 3 k-point grid was adopted for 2 × 2 × 2 supercell and the first Brillouin zone was divided into 2102 points. The corresponding band structure, total and partial density of state of SPE and SB_xPE x = 0.3, 0.5 phosphors were calculated, separately.

LEDs fabrication: To fabricate LED devices, 365 nm n-UV chips and as-prepared SB_xPE x = 0.3 were used for plant growth LED. For white LED, green emitting $(Sr,Ba)_2SiO_4:Eu^{2+}$ and red emitting $(Ca,Sr)AlSiN_3:Eu^{2+}$ phosphors were used as the additional green and red components. Certain amounts of these phosphors were weighted followed by well mixing with epoxy resin A and B (2 : 1, weight ratio) by hand. The obtained phosphor mixture was spread on n-UV chips and then transferred in an oven drying at 120 °C for 24 h to remove bubbles and solidify epoxy resin completely. The EL properties of the fabricated blue and white LEDs were tested on an automatic temperature control photoelectric analysis measurement system (ATA-500, Everfine)

Supplemental References

Blasse, G., and Grabmaier, B.C. (1994). Luminescent materials. Springer, Berlin, GER.

Chen, M.Y., Xia, Z.G., Molokeev, M.S., Lin, C.C., Su, C.C., Chuang, Y.C., and Liu, Q.L. (2017). Probing Eu^{2+} luminescence from different crystallographic sites in $Ca_{10}M(PO_4)_7:Eu^{2+}$ (M = Li, Na, and K) with β-$Ca_3(PO_4)_2$-type structure. Chem. Mater. *29*, 7536-7570.

Chen, M.Y., Xia, Z.G., Molokeev, M.S., Wang, T., and Liu, Q.L. (2017). Tuning of photoluminescence and local structures of substituted cations in $xSr_2Ca(PO_4)_2$–(1 – x)$Ca_{10}Li(PO_4)_7$:Eu^{2+} phosphors. Chem. Mater. *29*, 1430-1438.

Ji, X.Y., Zhang, J.L., Li, Y., Liao, S.Z., Zhang, X.G., Yang, Z.Y., Wang, Z.L., Qiu, Z.X., Zhou, W.L., Yu, L.P., et al. (2018). Improving quantum efficiency and thermal stability in blue-emitting $Ba_{2-x}Sr_xSiO_4$:Ce^{3+} phosphor via solid solution. Chem. Mater. 30, 5137-5147.

Kim, Y.H., Arunkumar, P., Kim, B.Y., Unithrattil, S., Kim, E., Moon, S.H., Hyun, J.Y., Kim, K.H., Lee, D., Lee, J.S., et al. (2017). A zero-thermal-quenching phosphor. Nat. Mater. *16*, 543-551.

Kresse, G., and Furthmüller, J. (1996). Efficient iterative schemes for ab initio total-energy calculations using a plane-wave basis set. Phys. Rev. B: Condens. Matter Mater. Phys. *54*, 11169.

Kresse, G., and Joubert, D. (1999). From ultrasoft pseudopotentials to the projector augmented-wave method. Phys. Rev. B: Condens. Matter Mater. Phys. *59*, 1758.

Liu, W.R., Huang, C.H., Wu, C.P., Chiu, Y.C., Yeha, Y.T., and Chen, T.M. (2011). High efficiency and high color purity blue-emitting $NaSrBO_3$:Ce^{3+} phosphor for near-UV light-emitting diodes. J. Mater. Chem. *21*, 6869-6874.

Mott, N.F., and Davis, E. (1979). Electronic processes in non-crystalline materials. Clarendon, Oxford, OX, UK.

Perdew, J.P., Burke, K., and Ernzerhof, M. (1996). Generalized gradient approximation made simple. Phys. Rev. Lett. *77*, 3865.

Qiao, J.W., Amachraa, M., Molokeev, M.S., Chuang, Y.C., Ong, S.P., Zhang, Q.Y., and Xia, Z.G. (2019). Engineering of $K_3YSi_2O_7$ to tune photoluminescence with selected activators and site occupancy. Chem. Mater. *31*, 7770-7778.

Qiao, J.W., Ning, L.X., Molokeev, M.S., Chuang, Y.C., Liu, Q.L., and Xia, Z.G. (2018). Eu^{2+} site preferences in the mixed cation $K_2BaCa(PO_4)_2$ and thermally stable luminescence. J. Am. Chem. Soc. *140*, 9730-9736.

Qiao, J.W., Zhou, G.J., Zhou, Y.Y., Zhang, Q.Y., and Xia, Z.G. (2019). Divalent europium-doped near-infrared-emitting phosphor for light-emitting diodes. Nat. Commun. *10*, 5267.

Van Uitert, L.G. (1984). An empirical relation fitting the position in energy of the lower d-band edge for Eu^{2+} or Ce^{3+} in various compounds. J. Lumin. *29*, 1-9.

Wang, C.Y., Takeda, T., Kate, O.M., Tansho, M., Deguchi, K., Takahashi, K., Xie, R-J., Shimizu, T., and Hirosaki, N. (2017). Ce-doped $La_3Si_{6.5}Al_{1.5}N_{9.5}O_{5.5}$, a rare highly efficient blue-emitting phosphor at short wavelength toward high color rendering white LED application. ACS Appl. Mater. Interfaces *9*, 22665-22675.

Wang, L., Wang, X.J., Takeda, T., Hirosaki, N., Tsai, Y.T., Liu, R-S., and Xie R-J. (2015). Structure, luminescence, and application of a robust carbidonitride blue phosphor ($Al_{1-x}Si_xC_xN_{1-x}:Eu^{2+}$) for near UV-LED driven solid state lighting. Chem. Mater. *27*, 8457-8466.

Wei, Y., Cao, L., Lv, L.M., Li, G.G., Hao, J.R., Gao, J.S., Su, C.C., Lin, C.C., Jang, H.S., Dang, P.P., et al. (2018). Highly efficient blue emission and superior thermal stability of $BaAl_{12}O_{19}:Eu^{2+}$ phosphors based on highly symmetric crystal structure. Chem. Mater. *30*, 2389-2399.

William, M.Y., Shigeo, S., and Hajime, Y. (2007). Measurements of phosphor properties. CRC, Boca Raton, FL, USA.

Yin, L.J., Dong, J.T., Wang, Y.P., Zhang, B., Zhou, Z.Y., Jian, X., Wu, M.Q., Xu, X., Ommenc, J.R., and Hintzend, H.T. (2016). Enhanced optical performance of $BaMgAl_{10}O_{17}:Eu^{2+}$ phosphor by a novel method of carbon coating. J. Phys. Chem. C *120*, 2355-2361.

Zhang, J.L., Zhang, W.L., Qiu, Z.X., Zhou, W.L., Yu, L.P., Li, Z.Q., and Lian, S.X. $Li_4SrCa(SiO_4)_2:Ce^{3+}$, (2015). A highly efficient near-UV and blue emitting orthosilicate phosphor. J. Alloys Compd. *646*, 315-320.

Zhang, S., Hao, Z.D., Zhang, L.L., Pan, G.H., Wu, H.J., Zhang, X., Luo, Y.S., Zhang, L.G., Zhao, H.F., and Zhang, J.H. (2017). Efficient blue-emitting phosphor $SrLu_2O_4:Ce^{3+}$ with high thermal stability for near ultraviolet (~400 nm) LED-Chip based white LEDs. Sci. Rep. *8*, 10463.

Zhang, X.G., Song, J., Zhou, C.Y., Zhou, L.Y., and Gong, M.Y. (2014). High efficiency and broadband blue-emitting $NaCaBO_3$: Ce^{3+} phosphor for NUV light-emitting diodes. J. Lumin. *149*, 69-74.

Zhao, M., Liao, H.X., Ning, L.X., Zhang, Q.Y., Liu, Q.L. and Xia. Z.G. (2018). Next-generation narrow-band green-emitting $RbLi(Li_3SiO_4)_2:Eu^{2+}$ phosphor for backlight display application. Adv. Mater. *30*, 1802489.